Journal of Biomedical Optics 9(1), 47–74 (January/February 2004)

Ultrahigh-resolution optical coherence tomography

Wolfgang Drexler
University of Vienna
Department of Medical Physics
Christian Doppler Laboratory
Vienna, Austria
E-mail: wolfgang.drexler@univie.ac.at

Abstract. In the past two decades, optical coherence tomography (OCT) has been established as an adjunct diagnostic technique for noninvasive, high-resolution, cross-sectional imaging in a variety of medical fields. The rapid development of ultrabroad bandwidth light sources has recently enabled a significant improvement in OCT imaging resolution, demonstrating the potential of OCT to accomplish its original goal of performing noninvasive optical biopsies, i.e., the *in vivo* visualization of microstructural morphology *in situ*, which had previously only been possible with histopathology. In addition, these novel light sources might also enable the use of spectroscopic OCT, an extension of ultrahigh-resolution OCT, for enhancing image contrast as well as detecting spatially resolved functional, biochemical tissue information. State-of-the-art-light sources that now permit ultrahigh-resolution OCT covering the whole wavelength region from 500 to 1600 nm are reviewed and fundamental limitations of OCT image resolution are discussed. *Ex vivo* ultrahigh-resolution OCT tomograms are compared with histological results; first clinical *in vivo* ultrahigh-resolution OCT and preliminary spectroscopic OCT results are presented and their impact for future clinical and research applications is discussed. [DOI: 10.1117/1.1629679]

Keywords: optical coherence tomography, ultrahigh resolution, ultrfast lasers, optical biopsy, medical diagnosis

Paper 103014 received Apr. 8, 2003; accepted for publication Jul. 1, 2003.

1 Introduction

New medical imaging technologies can improve the diagnosis and clinical management of a disease. Furthermore, they might also contribute to a better understanding of the pathogenesis and therefore to the development of novel therapies for a disease and thus have a significant, challenging impact in medical research and clinical practice. Minimally invasive imaging techniques have revolutionized diagnostic medicine during the past decades, e.g., X-ray computed tomography (CT),[1] magnetic resonance imaging (MRI),[2,3] functional magnetic resonance imaging (fMRI),[4] radioisotope imaging (position emission tomography, PET, and single-photon emission computed tomography, SPECT)[5] and diffuse optical tomography (DOT).[6] These techniques permit three-dimensional visualization; however, their spatial resolution is typically limited to a few millimeters in standard clinical practice. Optical imaging techniques such as conventional, confocal fluorescence as well as two- or multiphoton microscopy[7] enable high axial and transverse ($\leqslant 1$ μm) resolution imaging, but with only limited penetration and *in vivo* clinical diagnostic applications. In addition to biochemical methods, excisional biopsy and histopathology remain the gold standard for cancer diagnostics. However, in many instances, diagnostics based on biopsies suffer from high false negative rates because of sampling errors.

A- and B-scan ultrasonography is routinely used in ophthalmologic biometry and diagnosis to image and differentiate orbital disease and intraocular anatomy. These ultrasound measurements require physical contact with the eye and typically provide 150 μm of longitudinal resolution by using a 10-MHz transducer.[8,9] High-frequency (50 MHz) ultrasound can achieve an axial resolution of 20 to 30 μm, but its penetration depth is limited to 4 mm because of acoustic attenuation in ocular media.[10,11] Hence, only the anterior eye segment structures can be imaged with this high resolution. Scanning laser ophthalmoscopy or scanning laser tomography, invented in 1979, represented a major development in imaging of the ophthalmologic fundus.[12–14] A focused laser spot is raster scanned on the retina while measuring the integrated backscattered light to obtain high-quality, micron-scale lateral-resolution fundus images. Scanning laser ophthalmoscopy provides an en face view of the fundus, with high transverse resolution and contrast. However, pupil aperture and ocular aberrations limit the axial resolution in the retina to several hundred microns ($\sim$300 μm). Cellular-level real-time video imaging of the human cornea with submicrometer transversal resolution has been achieved by scanning slit confocal microscopy.[15,16]

In the past decade, advances in optics, fiber as well as laser technology have enabled the development of a novel noninvasive optical biomedical imaging technology, optical coherence tomography (OCT). It is analogous to conventional ultrasonic pulse-echo imaging, except that OCT does not require direct contact with the tissue that is being investigated and it measures echo delay and the intensity of backreflected infrared light rather than acoustic waves from internal tissue structures. Because the velocity of light is extremely high, direct measurement of optical echoes cannot be performed electronically as in ultrasound. Therefore OCT is based on a

1083-3668/2004/$15.00 © 2004 SPIE

classic optical measurement technique known as white light or low-coherence interferometery (LCI).[17–19] that enables noninvasive, high-resolution, *in vivo*, two- or three-dimensional cross-sectional imaging of microstructural morphology in transparent and nontransparent biological tissue *in situ*. Utilization of broad-bandwidth light sources in OCT permits tissue morphology to be imaged in detail at depths significantly greater than the penetration depth offered by conventional bright-field and confocal microscopy.

The eye is essentially transparent, transmitting light with only minimal optical attenuation and scattering and provides easy optical access to the anterior segment as well as the retina. Hence, optical ranging measurements, the optical analogue of ultrasound A-scans, were first demonstrated in 1986 using femtosecond light pulses as well as low-coherence interferometry.[19,20] Since then, two related versions employing a classic Michelson interferometer and a special dual-beam setup using an external interferometer have been developed for noninvasive ophthalmic high-precision and high-resolution biometry and tomography.[21–24]

By using dual-beam partial coherence interferometry, the first *in vivo* eye length measurements were achieved by Fercher and Roth.[19] The axial length of normal[25] and cataract eyes,[26] as well as corneal thickness and thickness profiles[27,28] were measured. A fully computer-controlled scanning version of the dual-beam version of OCT[29] has been developed, enabling biometry with 0.3- to 10-μm precision.[30] Its potential to perform noninvasive high-resolution biometry of intraocular distances with unprecedented precision has been utilized in studies of the cornea,[31] and intraocular lenses[32–34] as well as in research approaches to the effects of accommodation[35,36] and development in myopia.[37] Furthermore, it has been shown that use of this technique improves postoperative refractive outcome in cataract surgery by approximately 30%.[38–40] The high-precision biometry has also made it possible to determine the group refractive indices and the group dispersion of ocular media *in vivo*.[41] This dual-beam technique forms the basis of a commercial optical biometry instrument (IOLMaster, Carl Zeiss Meditec AG) that was successfully introduced to the market in 2000. Another challenging potential of this technique is its ability to perform tomographic imaging of the retina. The first *in vivo* tomogram of the human optic disk was reported in 1993 by Fercher et al.[42] using this technique. The first topographic measurements of the fundus of the human eye revealed the capability to quantitatively obtain the contours and the thickness profiles of retinal layers, with a precision of 2 to 3 μm.[29] Two-dimensional tomograms visualizing the microstructure of the retina have also been synthesized.[29,42,43]

By using a classic fiber optic Michelson interferometric setup,[11,12,44,45] Fujimoto et al.[22] presented the first *in vitro* tomogram of the human eye in 1991. Since then this version of OCT has advanced as a promising technique for both basic research and clinical applications. Several ophthalmic clinical studies have been conducted.[46] Besides the possibility of imaging the anterior eye segment[47,48] and morphological features of the human fovea and optic disk,[49] the detection and monitoring of a variety of macular diseases,[46,50] including macular edema,[51,52] macular holes,[53] central serous chorioretinopathy (CSC),[54] age-related macular degeneration (AMD) and choroidal neovascularization (CNV),[55] and epiretinal membranes[56] have been demonstrated. Furthermore, the thickness of the retinal nerve fiber layer (NFL), a possible predictor for early glaucoma, could be quantified in normal and glaucomatous eyes and correlated with conventional measurements of the optic nerve structure and function.[57,58] This prototype ophthalmic OCT system was developed into a clinical instrument, patented, and subsequently transferred to industry and introduced into the ophthalmic market in 1996 by Carl Zeiss Meditec Inc. of California. Since then, three generations of this instrument have been developed and successfully used in several clinical studies.[59–70] This version of OCT has now advanced to a powerful imaging technology in other medical fields because of its ability to perform cross-sectional, noninvasive subsurface imaging in highly scattering tissue for a large range of clinical diagnostic applications.[71–81] In addition, extensions of OCT technology, including Doppler flow[82–85] or polarization-sensitive[86–88] imaging, have been developed that provide spatially resolved imaging of velocity or birefringence.

Whereas several reviews have covered the historical development, fundamental theory, basic principles, technological extensions, and applications of OCT,[24,71,76,89–93] this paper reviews the fundamental principles of ultrahigh-resolution OCT,[94] a recently developed technology that produces a quantum leap in OCT imaging performance by significantly enhancing its axial resolution to the subcellular level. This unprecedented performance extends the original idea of OCT to noninvasive optical biopsy, i.e., the *in vivo* visualization of architectural tissue morphology *in situ* without excision of the investigated tissue, which had previously only been possible with histopathology. State-of-the-art-light sources, which enable ultrahigh-resolution OCT in the 500- to 1600-nm wavelength region are reviewed here, and fundamental limits of OCT image resolution are discussed. *Ex vivo*, first *in vivo* clinical ultrahigh-resolution OCT tomograms, and preliminary results of spectroscopic OCT, an extension of ultrahigh-resolution OCT for image contrast enhancement as well as the detection of spatially resolved functional and biochemical information on tissue, are also presented, and their impact for future clinical and research applications is discussed.

2 Key Technological Parameters of Optical Coherence Tomography

The performance of an OCT system is mainly determined by its longitudinal (axial) resolution, transverse resolution, dynamic range (i.e., sensitivity) and data acquisition specifications, including digitization resolution and speed. For application in medical diagnosis, additional factors, such as noncontact versus contact applicability, possible penetration into the investigated tissue, image contrast, and extraction of functional or biochemical information, in addition to the visualization of microstructural morphology, have to be considered. For clinical applications, compactness, user friendliness, robustness, flexibility, and overall costs of the OCT system, as well as the possibility of interfacing it with existing diagnostic technology are also decisive factors.

The major advantage of OCT for diagnostic imaging is that it may be performed using noninvasive or minimally invasive optical delivery systems, allowing repeated imaging to monitor the progression of a disease. Unlike ultrasound, OCT im-

aging can be performed directly through air, avoiding the need for direct contact with tissue or the requirement for a transducing medium, and therefore increasing the patient's comfort and minimizing the risk of infection. In addition, OCT can be performed in real time, allowing guidance of conventional excisional biopsy or investigation of dynamic response to therapeutic agents. OCT draws upon a well-developed fiber optic technology base and can therefore be easily interfaced with established medical diagnostic delivery systems (e.g., microscopes, slit lamps, fundus cameras, hand-held probes, and other standard medical delivery systems) to make noninvasive imaging possible.

Unlike technologies such as MRI or CT, OCT can be engineered into a compact, portable, and relatively inexpensive instrument, allowing low-cost screening and wide accessibility. Its major drawback compared with full-body imaging techniques is its limited penetration into nontransparent biological tissue. The maximum imaging depth in most tissues (other than the eye) is limited by optical attenuation and scattering to approximately 1 to 2 mm. This depth is shallow compared with other imaging techniques; however, the standard image resolution of OCT is more than ten times greater than that of conventional ultrasound, MRI, or CT. In addition, the imaging depth of OCT is sufficient for retinal imaging in ophthalmology. It is comparable to that typically sampled by excisional biopsy and is sufficient for the evaluation of most early neoplastic changes, which very often occur in the most superficial layers, e.g., the epidermis in the human skin or the mucosa and submucosa of internal organs.

2.1 *Longitudinal and Transverse Resolution*

In contrast to conventional and confocal microscopy, OCT achieves very high axial image resolution independent of focusing conditions because the axial and transverse resolutions are determined independently. The transverse resolution as well as depth of focus are governed by the focal spot size (as in conventional microscopy), while the axial resolution is mainly governed by the coherence length of the light source (rather than the depth of field, as in microscopy). The coherence length is the spatial width of the field autocorrelation measured by the interferometer. The envelope of the field correlation is equivalent to the Fourier transform of the power spectrum. The axial resolution is therefore inversely proportional to the spectral bandwidth of the light source, to $\Delta z = 2\ \ln(2)\lambda^2/(\pi\Delta\lambda)$, where $\Delta\lambda$ is the bandwidth and λ is the center wavelength of the light source used for imaging (assuming a Gaussian spectrum).

Figure 1 depicts this correspondence for the two standard wavelength regions used for OCT so far (800 nm and 1300 nm), assuming a Gaussian spectrum of the light source as well as a nondispersive imaging medium. It indicates that by using a light source with a 140-nm optical bandwidth at an 800-nm center wavelength, a free space resolution of approximately 2 μm can theoretically be achieved. It also indicates that for a further improvement by another factor of 2, down to 1 μm, the bandwidth of the light source must be doubled to 280 nm. This makes it very hard to achieve a longitudinal resolution in OCT imaging of less than 2 μm, because very broad bandwidth light sources are required. Figure 1 also shows that using a bandwidth of 180 nm centered at 800 nm enables a free space resolution of 1.6 μm. However, the same amount

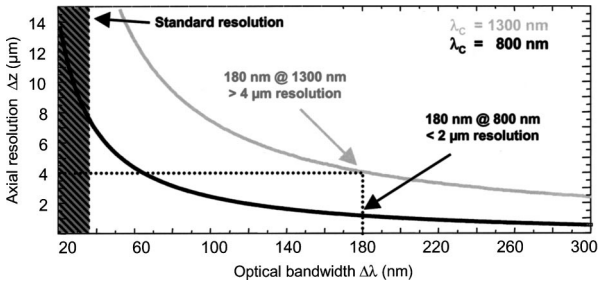

Fig. 1 Theoretical calculation of free space resolution (Δz at full width half maximum) as a function of the two standard wavelengths ($\lambda = 800$ and 1300 nm) used for OCT and optical bandwidth ($\Delta\lambda$). A Gaussian spectrum and nondispersive medium are assumed.

of bandwidth centered at 1300 nm enables only 4.1 μm. Hence even broader bandwidth light sources have to be used when employing light sources in the 1300-nm wavelength region. The actual resolution within the imaged tissue can be estimated by dividing the free space resolution, indicated by this figure, by the group refractive index, i.e., 1.35 to 1.4 for most biological tissues. It has to be noted that the axial resolution of OCT imaging is limited by dispersion of the sample, but also absorption and scattering within the sample, where photons with the same path but reflected from various imaging depths are detected.

An in conventional microscopy, the transverse resolution for OCT imaging is determined by the focused transverse spot size (defined as the $1/e^2$ radius of a Gaussian beam) of the optical beam, given by $\Delta x = (4\lambda/\pi)(f/d)$ where d is the spot size on the objective lens and f is its focal length. The transverse resolution is also related to the depth of focus or the confocal parameter $2z_R$ (two times the Rayleigh range): $2z_R = \pi\Delta x^2/2\lambda$. This implies that increasing the numerical aperture reduces the spot size, but also reduces depth of focus. High transverse-resolution OCT imaging can be achieved by focusing with a high numerical aperture at the expense of reduced depth of focus. This operating regime is similar to conventional microscopy or confocal microscopy, which has high transverse resolution but poor depth of field; for example, with a transverse resolution of 3 to 5 μm using a light source centered at 800 nm, a corresponding confocal parameter of only 35 to 100 μm in air can be achieved. To overcome this depth of field limitation caused by the high numerical aperture, C-mode scan imaging,[95] the use of special imaging lenses,[96] or dynamic focus tracking[97,98] can be used to maintain high transverse resolution throughout the whole penetration depth.

Especially for ophthalmic retinal OCT imaging, low numerical aperture focusing is employed because it is desirable to have a large depth of field and to use OCT to achieve high axial resolution. For a center wavelength of $\lambda = 800$ nm, a beam diameter of 2 to 3 mm, and neglecting the chromatic aberration of the human eye, the depth of field of the focus is approximately 750 μm, which is comparable to the depth over which retinal imaging is performed. However, low numerical aperture focusing yields a low transverse resolution. Studies have shown that the largest pupil size that still yields diffraction-limited focusing is approximately 3 mm, enabling theoretical retinal spot sizes of 10 to 15 μm.[99] The minimum

achievable transverse resolution for OCT is determined by the smallest achievable spot size on the retina. Using a reduced schematic eye for the optical analysis and diffraction-limited focusing of the eye, a 4-mm diameter beam at the pupil (with a center wavelength of 800 nm) would produce a theoretical spot size of 4.3 μm. In practice, however, for large pupil diameters, ocular aberrations limit this minimum focused spot size on the retina, even for monochromatic illumination. When ultrabroad bandwidth light is used, chromatic aberration will pose an additional limit to the smallest possible spot size. Furthermore, coma and other third-order aberrations, rather than spherical or fourth-order aberrations, appear to place the dominant limitation on the resolving power of the eye. One promising approach to correcting ocular aberrations in order to decrease the spot size at the human eye fundus and to therefore improve transverse resolution in OCT would be to use adaptive optics (AO).

The applications of AO have gone far beyond astronomy in the past decades. Correcting ocular aberrations was suggested in the early 1960s. With advances in technology, the first promising results were achieved in the late 1980s.[100] Today, deformable mirrors, liquid-crystal spatial light modulators, and phase plates have the potential not only for static, but also for dynamic correction of ocular aberrations.[101,102] Integrating this technique into ultrahigh axial-resolution ophthalmic OCT would enable even further improvement of the visualization possibilities of ophthalmic OCT. Combining AO with ultrahigh-resolution ophthalmic OCT should—besides providing an axial resolution of about 3 μm—enable a transverse resolution of about 5 μm. In addition, proper focusing onto the retina should also improve the sensitivity of the system through a more efficient collection of backscattered light.

2.2 *Dynamic Range, Sensitivity—Data Acquisition Speed*

OCT can achieve high detection sensitivity because interferometry measures the field rather than the intensity of light. Interferometric detection is a powerful approach for measuring the echo time delay of backscattered light with high sensitivity. This technique is closely related to heterodyne detection in optical communications. Weak backscattered optical signals are effectively multiplied by the reference signal. The signal-to-noise (SNR) performance of detection can be calculated from optical communication theory. The signal-to-noise performance is given as $SNR = 10 \lg(\eta P)/(E_p NEB)$, where P is the power that is reflected or backscattered, NEB, the noise equivalent power, is the bandwidth of the electronic detection, η is the photodetector efficiency, and E_p is the energy of the photon. This formula essentially states that the signal-to-noise performance is proportional to the power detected divided by the bandwidth measurement. This bandwidth is not the optical bandwidth of the light source, but instead refers to the electronic bandwidth or data acquisition rate. This formula also shows that there is a tradeoff between sensitivity, speed, and resolution. Furthermore, a minimum optical output of the light source employed is necessary in combination with an optimum system design[103,104] to enable near quantum-limited detection.

The specifications of optical coherence tomography systems vary widely according to their design and data acquisition speed requirements. A major limiting factor—especially for ultrahigh-resolution ophthalmic OCT—in dynamic range and sensitivity is the fact that the maximum allowed illumination power is limited by tissue or retinal exposure considerations. Superluminescent diodes, in contrast to femtosecond solid-state lasers, have the advantage of emitting laser light with extremely low-amplitude noise. In contrast, solid-state femtosecond lasers have excess amplitude noise that can decrease the signal-to-noise ratio and therefore the sensitivity of the system. Nevertheless, optimum imaging performance can still be obtained with these light sources to achieve nearly shot-noise-limited sensitivity by using dual-balanced detection.[105] Hence, typical OCT systems achieve detection sensitivities of 10^{-9} or 10^{-10} (-90 to -100 dB) of the incident optical power. This is sufficient to detect optical signals from depths of 1 to 2 mm in most scattering biological tissues.

Different approaches have been used so far to accomplish high-speed, real-time OCT imaging. The use of a rapid-scanning optical delay line[106] enabled *in vivo* video rate OCT imaging.[107] En face OCT uses rapid transverse scanning to achieve high-speed OCT imaging with large voxels per second acquisition rates.[108] Two other alternatives for high-speed OCT imaging are parallel OCT using a smart detector array[109] or Fourier domain OCT.[110,111]

2.3 *Center Wavelength, Penetration, and Image Contrast*

OCT imaging at different wavelengths can be used to enhance tissue contrast and penetration, as well as to measure absorbing or scattering properties of various pigments and structures. Tissue scattering and absorption properties are strongly dependent upon tissue morphology, such as cell and nuclei size, shape, and density, as well as the physiological state of certain chromophores. Hence, OCT penetration depth is significantly affected by light scattering within biological tissue, which is scaled as $1/\lambda_c^k$, where the coefficient k is dependent on the size, shape, and relative refractive index of the scattering particles.[89] The difference in tissue scattering and absorption provides structural contrast for OCT. Image contrast can be enhanced by the use of polarization-sensitive OCT,[86–88] phase-contrast OCT,[112,113] or by using spectroscopic OCT. Most biological tissues absorb in the visible and near-IR wavelength range because of the presence of hemoglobin and melanin. In the range between 0.8 and 1.8 μm, scattering is the predominant mechanism limiting image penetration depth. Since scattering depends strongly on wavelength and decreases for longer wavelengths, significantly better image penetration depth can be achieved with light centered at 1.35 μm than at 0.85 μm. It has been shown that the optimum wavelengths for imaging in biological tissues are in the 1.3 to 1.5-μm range. In this range imaging depths of 1 to 2 mm can be achieved.[114,115] Water absorption becomes a problem for wavelengths >1.8 μm. A strong water absorption peak at ~ 1.43 μm can also modulate the spectral width of a broad bandwidth light source centered at 1.3 μm, as a function of depth in biological tissue, since most soft tissues have 50 to 90% water content. Hence, if the center wavelength and bandwidth of the coherent light source used for OCT could be chosen across the range from 500 to 1500 nm, axial resolution

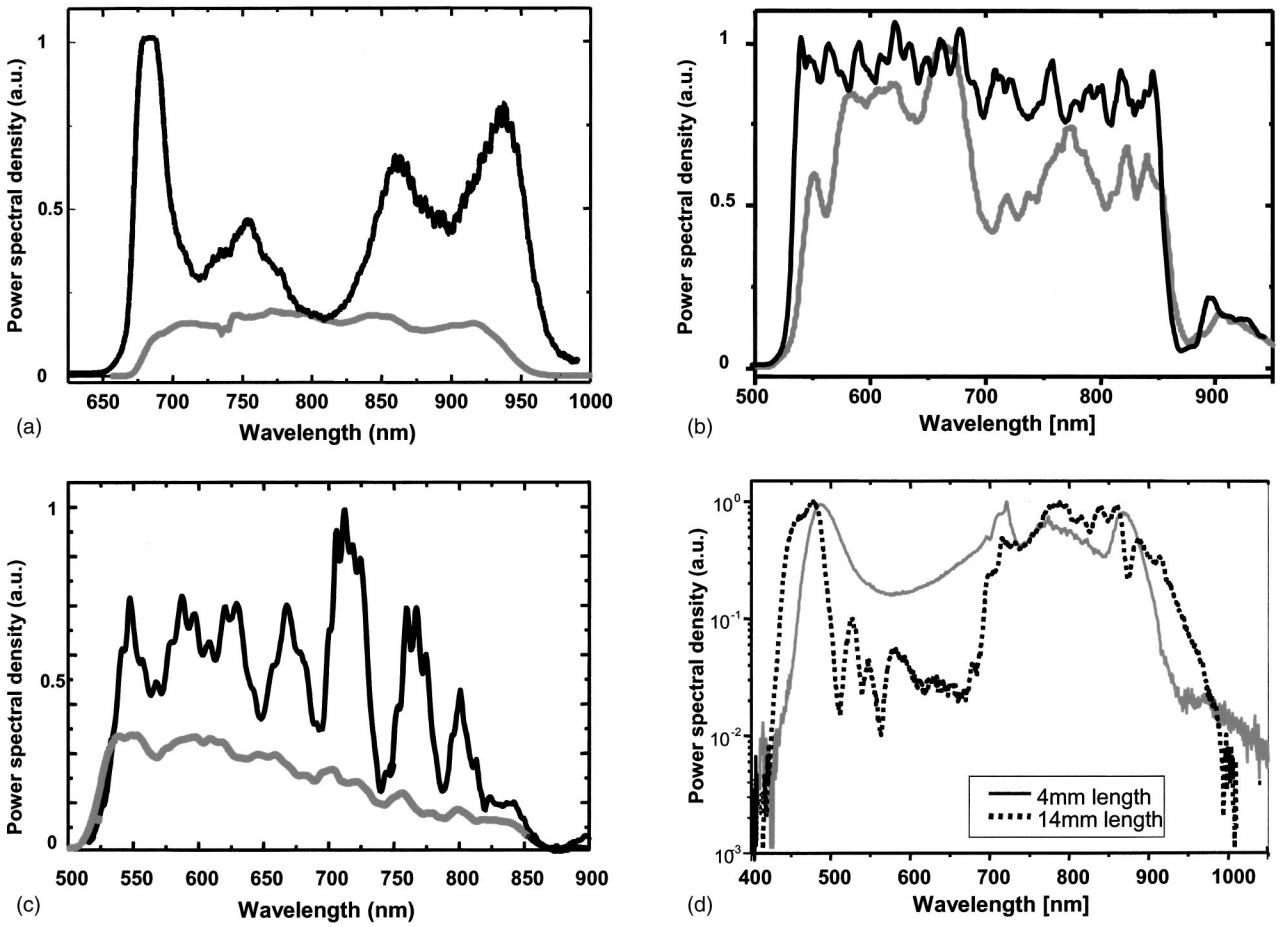

Fig. 2 Spectral shaping methods; black lines indicate original spectrum, gray lines indicate shaped spectrum. (a) Shaping by introducing wavelength-dependent attenuation. (b) and (c) Effect of liquid-crystal-based spatial light modulator. (d) Optimizing input pulse parameters in supercontinuum generation with photonic crystal fibers (PCF); in this case the PCF length has been optimized.

and contrast as well as penetration could be optimized according to the imaging procedure and medical application.

3 Axial Resolution Limits for Ultrahigh-Resolution OCT

3.1 *Spectral Shape of Ultrabroad Bandwidth Light Sources*

The necessary light source specifications for ultrahigh-resolution OCT are not only spatially coherent, ultrabroad bandwidth emission with enough output power and good amplitude stability, but also optimum spectral shape. Since the coherence length is defined as the full width at half maximum (FWHM) of the field autocorrelation measured by the OCT interferometer, the width and also the shape of the coherence function of an OCT system is dependent on the spectral shape of the light source as well as on the transfer function of the OCT system. The latter is mainly determined by the optical properties of the interferometer, e.g., wavelength-dependent losses and splitting ratios of beamsplitter and lenses, as well as the cutoff wavelength of the single-mode fibers employed and the wavelength-dependent sensitivity of the photodetectors employed. The ideal spectrum for OCT would have a Gaussian spectral shape, resulting in a Gaussian coherence function with no side lobes. Large spectral modulations would reduce sensitivity and resolution, owing to the presence of side lobes in the fringe pattern that appear symmetric to the maximum of the coherence functions.

There are several possibilities for changing the shape of the emission spectrum of the light source used. The easiest way is to introduce an optical dichroic or interference filter that suppress certain wavelength regions. Another possibility is to spatially disperse the optical beam with prisms and to induce local and therefore wavelength-dependent losses by introducing razor blades or thin objects into the dispersed light beam. Figure 2(a) demonstrates the effect of this shaping method when applied to a strongly modulated spectrum of an ultrabroad bandwidth titanium:sapphire (Ti:sapphire) laser. Alternatively, the configuration of this prism can be used in combination with a liquid-crystal spectral amplitude or phase shaper (spatial light modulator), a well-established technique for pulse-shaping applications in ultrafast optics.[116] With this technique, selected wavelength regions of less than 10 nm can be attenuated by a factor of up to 80%. Figures 2(b) and 2(c) demonstrate the capabilities of this technique. Note that this technique is rather expensive and more challenging concerning the control of the 640 liquid-crystal elements. In addition, spectral shapers introduce power losses of up to 50%. In the case of light sources that are based on nonlinear optical ef-

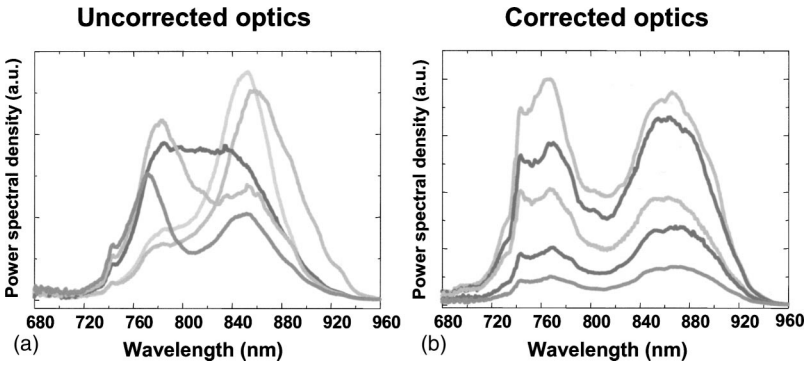

Fig. 3 Effect of chromatic aberration. Optical spectra at the exit of an OCT interferometer. Spectra are displayed as a function of focusing distance onto a mirror in the sample arm, employing (a) a standard (not achromatic) as well as (b) an optimized achromatic lens in the sample arm. Standard lenses introduce spatially changing effective optical bandwidths and therefore spatially changing axial resolution.

fects in special fibers, the proper choice of the input pulse parameters into the fiber can be used for spectral shaping of the output spectrum generated.[117] Figure 2(d) depicts an example where the fiber length that has been used to generate a supercontinuum has been optimized to minimize spectral modulations. By carefully optimizing the pulse input parameters, emission spectra with up to 325 nm could be generated with less than 1.5 dB modulations directly out of the fiber, with no additional spectral shaping (cf. Sect. 4.3).

3.2 *Chromatic Aberration Limitations to Resolution*

Another limitation for achieving ultrahigh resolution is the chromatic aberration of the optics employed. Conventional lenses have a focal length that varies with wavelength and thus they focus ultrabroad bandwidth light an different focal positions. This variation in focal position for different wavelengths limits the actually effective bandwidth and therefore degrades resolution. Figure 3 depicts a comparison of spectra at the exit of an ultrahigh-resolution OCT interferometer for different focal distances when standard—uncorrected—optics [Fig. 3(a)] and specially designed optics with minimal chromatic aberrations [Fig. 3(b)] is used in the sample arm. It is obvious that for different focal distances of the uncorrected optics [Fig. 3(a)], a different actual spectrum is effective, resulting in different actually effective bandwidths at full width at half maximum and therefore a spatially changing axial resolution. In the case of a specially corrected achromatic optics, different focal distances just introduce a wavelength-independent attenuation of the whole spectrum, maintaining the spectral shape, optical bandwidth, and therefore axial resolution. Hence, appropriately coated and designed achromatic objectives have to be used to maintain the ultrabroad bandwidth of the light in order to achieve ultrahigh resolution. Alternatives are catadioptic (reflective) objectives of parabolic mirrors that have minimal chromatic aberration and do not introduce any dispersion. For ophthalmic OCT, since the human eye is not a diffraction-limited optical system, chromatic aberration in the eye itself may ultimately limit the axial resolution of ultrahigh resolution retinal OCT imaging.

3.3 *Group Velocity Dispersion Limitations to Resolution*

As mentioned before, the axial resolution of OCT is mainly determined by the bandwidth of the low-coherence light source. However, chromatic (or group velocity) dispersion is another limiting factor that degrades resolution by broadening the axial point spread function. Chromatic or group velocity dispersion causes different frequencies in the broad bandwidth light to propagate with different velocities. It should be noted that the group velocity dispersion changes the phase but not the bandwidth of optical signals. The axial point spread function, i.e., the interferometric autocorrelation function, will also broaden and therefore decrease resolution if there is a significant mismatch in the dispersion of group velocity between the reference and the sample arms of the measurement system. Both the fiber optics and the sample itself (especially in the case of the human eye) may have significant dispersion. The effect of broadening will become more severe with increasing optical bandwidth and thickness of the sample and is less pronounced for longer wavelengths. A dispersion mismatch between the interferometer arms of the OCT system also degrades the peak height of the interference envelope, which reduces the system's dynamic range.

In order to compensate for these effects, dispersion can be compensated by using a numerical a posteriori depth-variant dispersion compensation, or dispersion introduced by the fiber length and optics mismatch between the sample and the reference arm can be carefully balanced by using variable thicknesses of fused silica (FS) and BK7. This dispersion balancing can be done in real time by performing fast Fourier transform (FFT) analysis of the interference signal of a single reflecting site sample. The thickness of fused silica and BK7 in the reference arm can be changed systematically until a uniform group delay dispersion, i.e., the first derivative of the phase that has been obtained by FFT, is achieved. Figure 4 illustrates this real-time dispersion balancing technique. It shows interference fringes detected when using a single reflecting sample [e.g., a mirror Fig. 4(a)], corresponding spectrum [Fig. 4(b)], the derived group delay [Fig. 4(c)], and group delay dispersion [Fig. 4(d)]. For ultrahigh-resolution retinal OCT imaging, the dispersion of approximately 25 mm

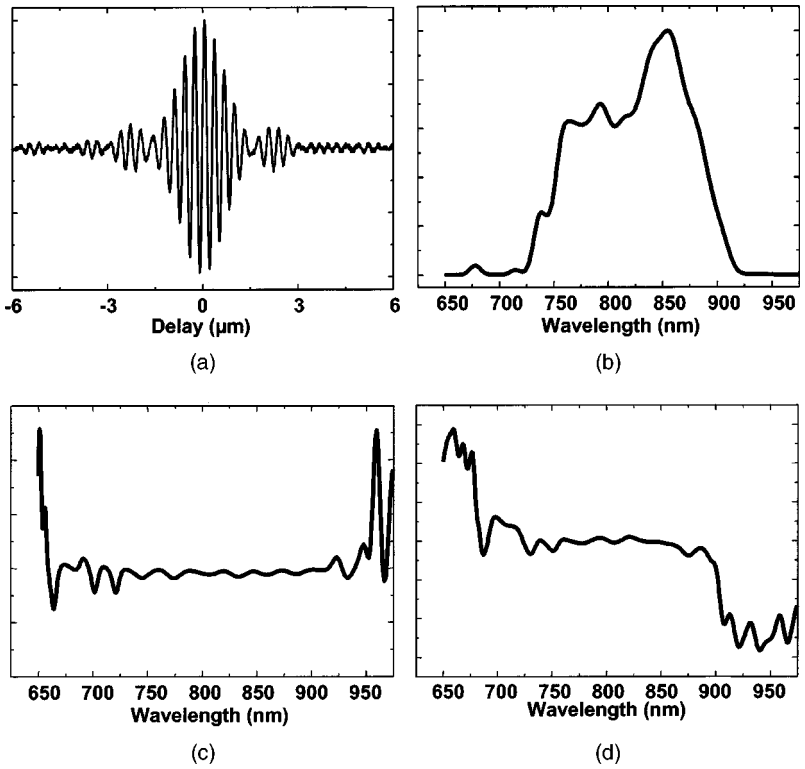

Fig. 4 Online OCT system dispersion compensation. (a) Interference fringe signal detected from a mirror in the sample arm. (b) Spectrum obtained by Fourier transformation. (c) Group delay from the first derivative from the phase, indicating a dispersion match or mismatch. (d) Group delay dispersion from the second derivative of the phase, indicating a higher-order dispersion mismatch.

of ocular media can be compensated by using 25 mm of water in the reference arm, since previous *in vivo* studies of dispersion measurements have shown that the dispersion of ocular media averaged over 25 mm is similar to that of 25 mm of water.[41]

Balancing the higher-order dispersion distribution of the 25-mm ocular media in front of the retina is more critical for obtaining high resolution than balancing the dispersion of the system itself. Figure 5 and Fig. 6 demonstrate this effect. The dispersion-balanced [Fig. 5(a)] and unbalanced [Fig. 5(b)] interference signal of double-passing 25 mm of water is depicted in Fig. 5. Resolution degrades from 4 μm to 52 μm, or more than a factor of 10. Figure 6 depicts the effect of dispersion mismatch in the case of *in vivo* ultrahigh-resolution retinal imaging of a normal human fovea [Fig. 6(a)]. By artificially introducing dispersion mismatch by inserting 3 mm [Fig. 6(b)] and 9 mm [Fig. 6(c)] of fused silica in the reference arm of the OCT interferometer, it is obvious that both OCT resolution and sensitivity (up to -5 dB) decrease. Clinical application of ultrahigh-resolution ophthalmic OCT revealed that by using a dispersion compensation of 25 mm of water in the reference arm of the interferometer, patients with an axial eye length between 23 mm and about 27 mm can be

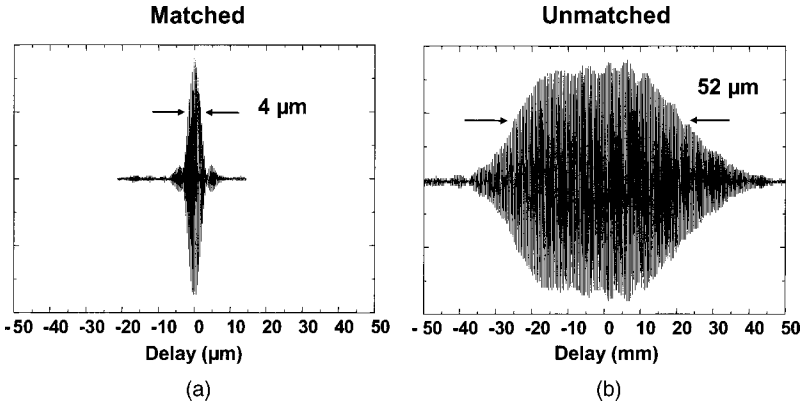

Fig. 5 Dispersion balanced (a) and unbalanced (b) interference signal after double-passing 25 mm of water, introducing a dispersion that is the same thickness as ocular media. Resolution degrades by more than 10 times.

imaged without any significant loss of axial resolution induced by a dispersion mismatch.

3.4 *Other Limitations to Resolution*

Another effect that limits axial OCT resolution in ultrahigh-resolution OCT systems is a polarization mismatch between the interferometer arms, which introduces a phase difference and therefore a change in the shape of the coherence function and axial resolution, respectively.

The optical transmittance, coating, and wavelength-dependent losses of the bulk or fiber optics employed, the delivery system optics, and the human eye itself—in the case of ultrahigh-resolution ophthalmic OCT—strongly influence the axial resolution as well as the sensitivity of the OCT system. Single-mode fibers with appropriate cutoff wavelengths have to be used to provide single-mode light propagation. Conventional fiber couplers are designed to maintain 3-dB splitting over a wavelength range of typically ± 10 nm. By using these fiber couplers for delivery of broad-bandwidth laser light, unequal beam splitting with respect to wavelength and power can occur and will reduce resolution. Hence special broad-bandwidth, wavelength-flattened, 3-dB fiber or bulk optic beamsplitters have to be used to maintain broad bandwidths and consequently high axial resolution. It is important to note that bidirectionality of bulk or fiber-based beamsplitters is important in order not to introduce wavelength-dependent losses on the way back to the detector.

The detection system, including the electronics as well as the digitization and acquisition of the interference signal, have to be designed properly to avoid degradation of axial OCT resolution. Hence, the transimpedance amplifier, but more particularly the electronic bandpass filtering, must be designed properly and adapted to the ultrabroad optical bandwidth. The electronic bandwidth of the bandpass must not be so narrow as to reduce the axial resolution, but must also not be so broad that it reduces sensitivity by introducing noise. Real-time adaptive filtering might be a proper approach to optimize sensitivity and maintain axial resolution. In addition, hardware demodulation must be adapted to the scanning speed and optical bandwidth to avoid broadening caused by the time response of the electronics used, resulting in a larger coherence length of the envelope compared with to the full interference fringe signal. Finally, the signal must be temporally digitized correctly with at least 5 to 10 times oversampling in respect to central wavelength, Doppler shift, and scanning speed to not degrade the achieved axial resolution by undersampling. For high-speed ultrahigh-resolution OCT, data acquisition boards with 16-bit or at least 12-bit resolution as well as 5 Megasamples/second or even 10 Megasamples/second or more are therefore necessary.

Finally, the mechanical performance of the scanners used for transverse and depth scanning has to be accurately selected and correctly controlled. Mechanical jitter or displacement of adjacent depth scans as well as noisy control signals of the scanner might result in distorted and therefore resolution-degraded ultrahigh-resolution OCT tomograms.

4 Broad-Bandwidth, Low-Coherence Light Sources for Ultrahigh-Resolution OCT

The significant difference between OCT and conventional microscopy is that OCT achieves very high axial image resolutions independent of focusing conditions, because the axial and transverse resolution are determined independently by different physical mechanisms. This implies that axial OCT resolution can be enhanced using broad-bandwidth, low-coherence length light sources. It is important to note that the light source not only determines axial OCT resolution via its bandwidth and central emission wavelength, but also determines both the penetration in the sample (biological tissue) and the OCT transverse resolution. A minimum output power with low-amplitude noise is necessary to achieve high sensitivity and high-speed, real-time OCT imaging. Furthermore, ultrabroad-bandwidth light sources emitting in different wavelength regions might also make a potential extension of OCT possible, e.g., spectroscopic OCT. Hence it is obvious that the light source is *the* key technological parameter for an OCT system, and a proper choice is imperative.

The longitudinal resolution of current OCT systems is limited by the optical bandwidth of the light source. Typically these are superluminescent diodes (SLDs) with 20 to 30 nm and a yield of about 10 to 15 μm, providing more detailed structural information than any other standard imaging technique. However, the resolution is significantly below what can be achieved technically and is insufficient to identify individual cells or to assess subcellular structures such as nuclei or mitotic figures. Owing to the lack of powerful, broad-bandwidth, spatially coherent light sources, OCT imaging has been mainly performed so far in the 800- and 1300-nm wavelength region.

Incandescent sources, although broad bandwidth, produce very little intensity in a single spatial mode. Nevertheless some research groups have explored these broadband light sources for improvement of the axial imaging resolution by employing a technique that uses a multitude of mutually incoherent low-coherence interferometry channels in order to increase the probe beam power[118] or by using a Linnik-type interference microscope in combination with a CCD camera-based parallel detection scheme.[119] Figure 7(a) depicts a typical spectrum using the latter technique, employing a 100-W tungsten halogen lamp in a Köhler illumination system and the corresponding coherence function [Fig. 7(b)], achieving 1.9-μm free space axial resolution. The advantage of this technique is that it uses a low-cost light source and a compact OCT system, and can achieve a data acquisition speed of up to 200 frames per second. Its major drawback, though, is the low brightness, which limits the sensitivity and applicability of this technique for *in vivo* OCT imaging in a clinical setting. Figures 7(c) and 7(d) are typical tomograms of an onion obtained with this technique and the corresponding histology [Fig. 7(e)].

4.1 *Ultrabroad-Bandwidth Light Sources in the 800-nm Wavelength Region*

The first axial resolution lower than 10 μm was achieved by using broadband fluorescence from organic dye[120] and from a Ti:sapphire laser.[121] However, biological imaging could not be performed with these light sources because of their low brightness. Recently a superluminescent Ti:sapphire crystal was demonstrated as a simple and robust alternative to achieve a sub-2-μm axial resolution in OCT.[122] The drawback of this light source is that it has to be pumped by an expensive

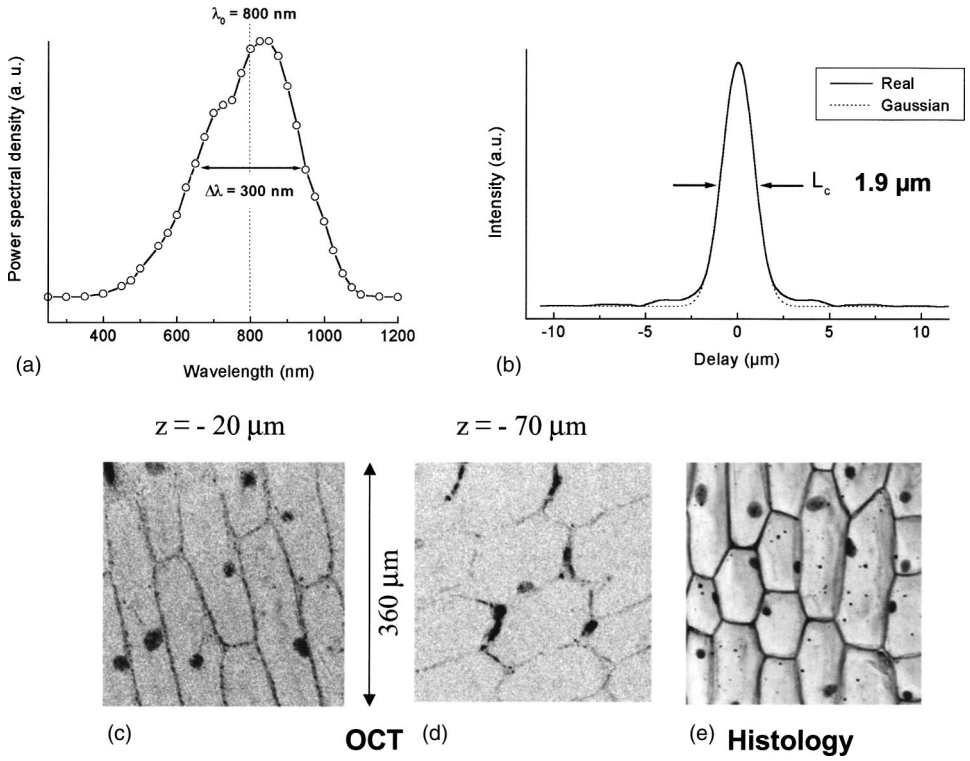

Fig. 7 (a) Typical spectrum using a 100-W tungsten halogen lamp in a Köhler illumination system and (b) the corresponding coherence function, achieving 1.9-μm free space axial resolution. (c) and (d) Typical tomograms of an onion obtained with this technique and (e) corresponding histology (with permission of Prof. Dr. C. Boccara and Dr. A. Dubois, Laboratoire d'Optique, Paris.)

5-W frequency-doubled, diode-pumped laser to achieve only 40 μW of output power. Hence this light source is still neither a low-cost alternative nor suitable for *in vivo* clinical high-speed, ultrahigh-resolution OCT imaging. Besides the standard specifications of about 20 to 30 nm bandwidth FWHM centered in the 800- to 850-nm wavelength region, providing about 10 to 15 μm of axial OCT resolution, superluminescent diodes with up to 70-nm bandwidths (FWHM), typically centered at 830 nm with about 3-mW fiber pigtailed output power are also commercially available.[123] The spectrum of these SLDs is modulated in a double hump shape, which is also forward-current dependent. By multiplexing spectrally displaced superluminescent diodes to increase the optical bandwidth,[124–126] improved-resolution OCT tomograms with about a 7-μm resolution in the retina have been demonstrated.[127] Recently reported cost-effective approaches for broad-bandwidth light sources mainly take advantage of the lower power demand with ultrahigh-resolution OCT imaging.[128–131] The limiting factors of these systems are the relatively small bandwidths for ultralow-pump-threshold Kerr-lens modelocked (KLM) Ti:sapphire lasers and the strongly modulated spectra of Cr^{3+}-ion lasers; thus they are not perfectly suitable for OCT.

Today, ultrashort light pulses produce the shortest, controlled, technically produced events. This can be demonstrated by the fact that a single femtosecond compared to a second is equivalent to 5 min compared to the age of the universe. Femtosecond laser development has concentrated so far mainly on the temporal features of the pulses, which were often optimized to the detriment of the spectral shape. In OCT, the pulse duration is irrelevant, while the spectral width and shape play a crucial role. However, unlike ultrafast femtosecond time-resolved measurements where special care must be exercised to maintain the short pulse duration, OCT measurements depend on field correlations rather than intensity correlations. Field correlation is preserved even if the pulse duration is long. Femtosecond mode-locked solid-state lasers can generate ultrabroad-bandwidth, low-coherence light with a single spatial mode and high power, providing both high resolution and the high power necessary for high-speed OCT imaging. These lasers can operate over a broad range of wavelengths that are desirable for ultrahigh resolution as well as spectroscopic OCT imaging in tissue. In a first approach, a Ti:sapphire laser has been used for *in vitro* OCT imaging in nontransparent tissues with a 4-μm axial resolution.[132]

In preliminary studies, an OCT system was developed and could be optimized to support 260 nm of optical bandwidth from a state-of-the art Ti:sapphire laser.[133] This laser was developed in collaboration with other investigators at Massachusetts Institute of Technology and generated pulses of $<$5.5 fs duration, corresponding to bandwidths of more than 350 nm at an 800-nm center wavelength.[134] This high performance was achieved using specially designed double-chirped mirrors with a high reflectivity bandwidth and controlled dispersion response. Figure 8 shows a comparison of the spectra and resolution of an OCT A-scan using a conventional superluminescent diode light source versus the femtosecond Ti:sapphire laser source. The ultrabroad bandwidths generated by the femtosecond laser allow the axial resolution of OCT to be improved by a factor of nearly 10 over standard OCT technol-

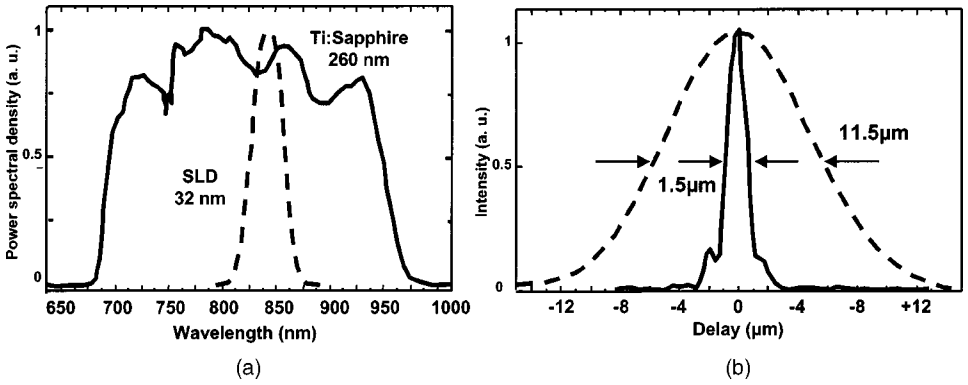

Fig. 8 Solid-state laser light sources make ultrahigh resolution and spectroscopic OCT imaging possible. (a) The spectrum of the Ti:sapphire laser versus a standard superluminescent diode (SLD) is shown, depicting their respective wavelength bandwidths. (b) A demodulated OCT axial scan showing the axial resolution of OCT using Ti:sapphire (solid) versus SLD (dashed) light sources. Solid-state lasers provide almost a 10 times improvement in resolution.

ogy. This femtosecond laser source has been used for imaging studies using an OCT microscope as well as an ophthalmic system interfaced to a biomicroscope system.

Figure 9 demonstrates the feasibility of this novel OCT system for three-dimensional *in vivo* subcellular imaging of a *Xenopus laevis* (African tadpole) mesenchymal cell. A total of eighteen tomograms spaced 2 μm apart of an area 70 $\times$50 μm, covering approximately half of the cell, have been imaged at 1$\times$3 μm (length$\times$width) resolution, consisting of 170$\times$100 pixels and 0.4$\times$0.5-μm pixel spacing. The back surface of the cell (at 0 μm), cell membranes, and nuclei as well as intracellular morphology (at 20 to 26 μm) can be visualized. Preliminary results of an *in vivo* optical biopsy using ultrahigh-resolution retinal OCT imaging in human subjects have demonstrated for the first time the visualization and quantification of intraretinal structures.[135,136]

These preliminary results were obtained with an ultrahigh OCT system that is based on a complex laboratory laser system that is not suitable for clinical studies. Therefore a new generation of a compact ultrahigh-resolution OCT system was developed in collaboration with the Photonics Institute of the Technical University of Vienna and FEMTOLASERS Produktions GmbH, Vienna, Austria. This system consists of a high-speed scanning unit (up to 250 Hz, 400 mm/s) integrated in a fiber optics-based Michelson interferometer employing a compact, user-friendly, state-of-the-art sub-10 fs Ti:sapphire laser [Femtosource Compact Pro, FEMTOLASERS [Fig. 10(a)], 800-nm center wavelength, up to 165-nm (FWHM) optical bandwidth [Fig. 10(b)], 400-mW output power. The interferometer was interfaced with a microscope delivery system. Both the fiber optic interferometer and the optical components of the microscope were designed to support the propagation of very broad bandwidth light throughout the OCT system and to compensate for any polarization and dispersion mismatch between the sample and reference arms of the interferometer.

In order to achieve high transverse resolution, a specially designed achromatic objective with a 10-mm focal length and a numerical aperture of 0.25 was used to achieve 3-μm free space transverse resolution. To overcome the depth-of-field limitation and to maintain high transverse resolution at varying depths through the image, a zone focus and image fusion technique were used. Applying laser light centered at 800 nm with up to a 165-nm bandwidth (FWHM), an axial resolution

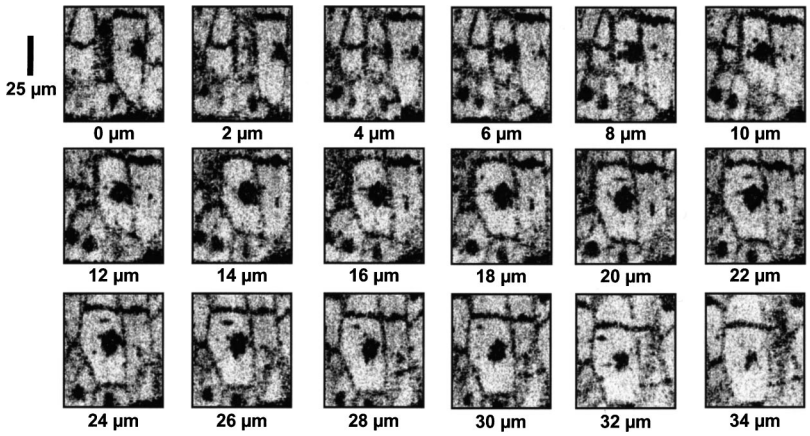

Fig. 9 Eighteen *in vivo* ultrahigh-resolution (1$\times$3 μm; axial$\times$transverse) tomograms spaced 2 μm apart with 1$\times$3-μm resolution of half of a *Xenopus laevis* (African tadpole) mesenchymal cell. The cell membrane and cell nuclei as well as intracellular morphology (e.g., at 20 to 26 μm) can be visualized.

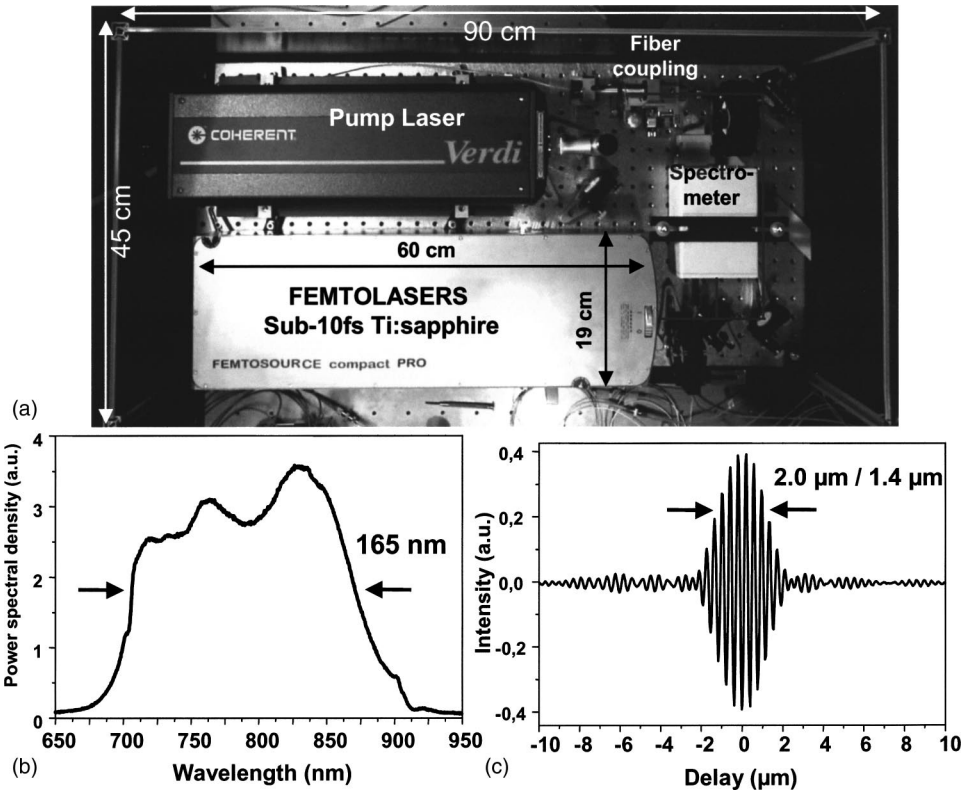

Fig. 10 (a) Schematic diagram of a compact, commercially available Ti:sapphire laser (Fem Tosource Compact Pro, FEMTOLASERS GmbH). (b) Typical optical output power spectra of this Ti:sapphire laser and (c) corresponding interference signal that makes possible a free space axial resolution of 2 μm, corresponding to 1.4 μm in biological tissue.

of 2.0 μm in air, corresponding to 1.4 μm in biological tissue, has been achieved with this system [Fig. 10(c)]. A signal-to-noise ratio of 105 dB was achieved at a 1-MHz carrier frequency by using an incident power of 5 mW employing dual-balanced detection. Full interference fringe signal OCT data were digitized with a high-speed (10 Ms/s) and high-resolution (16-bit) analog-to-digital (A/D) converter following software demodulation.

As a first step, *ex vivo* pig and monkey (*Macaca fascicularis*) retinal specimens were acquired to correlate ultrahigh-resolution OCT images with histology and to provide a basis for improved interpretation of *in vivo* ophthalmic OCT tomograms of high clinical relevance.[137] Pig retinas have an anatomy similar to that of humans; monkey retinas are identical to human retinas. For exact interpretation of OCT tomograms and correlation to histology, it is important to use fresh retinal specimens. Pig retinas were therefore chosen because of their easier availability within 1 to 2 h postmortem compared with human retina samples. Pig retinal samples were immediately preserved in buffered solutions to maintain osmolarity and oxygen support; monkey retinal samples were perfusion fixed. Figure 11 shows an example of an ultrahigh-resolution OCT image of a pig retina 2 h postmortem acquired with 1.4-μm axial and 3-μm transverse resolution. The image dimensions are 0.7×2 mm, with $20{,}000\times2000$ pixels. Enlargements show the clear visualization of nerve fiber bundles, Müller cell arcades, and all major intraretinal layers. Furthermore, the high axial resolution allows clear identification of areas of detached and nondetached retina to the choriocapillaris, which is extremely important for ophthalmic diagnosis.

Figure 12 shows a comparison of *in vitro* ultrahigh-resolution OCT imaging (a) with histology (b) using a differential interference contrast (DIC) micrograph of a frozen section obtained from the matching retinal position in the pig retina. From the proximal (top) to the distal (bottom) retina, alternate dark and light bands of signal in the OCT image directly correlate with the retinal layers, nerve fiber layer (NFL), ganglion cell layer (GCL), inner plexiform layer (IPL), inner nuclear layer (INL), and outer plexiform layer (OPL). Distal to a band attributable to the outer nuclear layer (ONL), a more delicate bright layer is likely to represent both the external limiting membrane and the myoid portion of the cone inner segments (IS). The adjacent dark and stippled signal is in alignment with the cone ellipsoids prominently seen using DIC optics. A distal dark band is possibly associated with the cone outer segment tips and, finally, the dark and light banding is attributable to the pigment epithelium–choriocapillaris complex.

Figure 13 shows a comparison of *in vitro* ultrahigh-resolution OCT imaging [Fig. 13(a)] with the histology [Fig. 13(b)] of a papillomacular scan of a monkey retina, demonstrating excellent correlation. Figure 14 demonstrates the ability of ultrahigh-resolution OCT to visualize specific morphological features such as the epithelium, Bowman's layer, and Descement's membrane and endothelium in addition to the typical stromal structure in a human cornea 4 days postmortem.

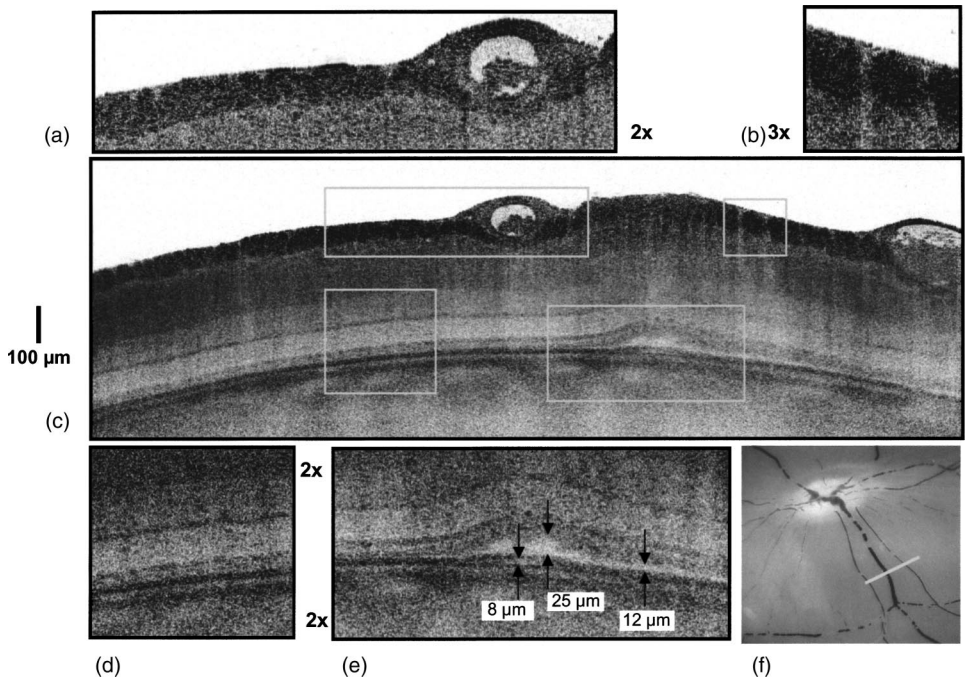

Fig. 11 Ultrahigh-resolution OCT image (1×3 μm; axial×transverse resolution) of a pig retina 2 h postmortem. The enlargements indicate (a) and (b) nerve fiber layer regions, (d) intraretinal layers, (e) retinal detachment, and (f) OCT scan location.

Recently, a compact, clinically viable ultrahigh-resolution (~3 μm) ophthalmic OCT system has been developed and used in clinical imaging for the first time.[138] In this study, a compact, robust, commercially available Ti:sapphire laser (Compact Pro, FEMTOLASERS) with up to a 165-nm bandwidth at an 800-nm center wavelength was used. This ultrahigh-resolution OCT system is based on a commercially available OCT system (OCT 1) that was provided by Carl Zeiss Meditec, Inc. OCT imaging was performed with axial scan rates up to 250 Hz using up to 800 μW of incident power in the scanning OCT beam, which is well below the ANSI exposure limits. To date, more than 250 eyes of 160 patients with different macular diseases, including macular hole, macular edema, age-related macular degeneration, central serous chorioretinopathy, epiretinal membranes, detachment of pigment epithelium and sensory retina, glaucoma, and different hereditary retinal diseases have been examined. Figure 15 shows the appearance of the photoreceptor (PR) and outer nuclear layer (ONL) as well as external limiting membrane (ELM) in a normal human retina compared with different macular pathologies. In the extreme case of Stargadt dystrophy, the PR, the ONL, and the ELM appear completely degenerated, whereas in different stages of macular hole the PR layer as well as the ELM seem to be less affected in early stages (cf. macular hole 1 with later stages, macular holes 2 and 3). A displacement of the PR layer as well as the ELM

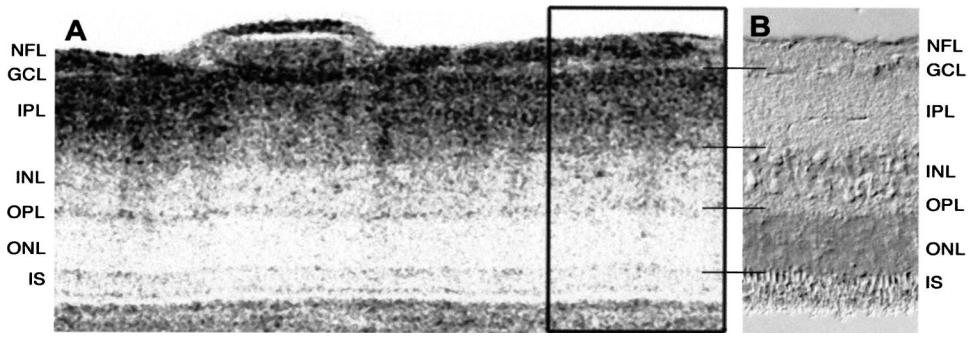

Fig. 12 Comparison of (a) *in vitro* ultrahigh-resolution OCT imaging (1×3 μm; axial×transverse) with histology and (b) differential interference contrast (DIC) micrograph of a frozen section obtained from the matching retinal position in the pig retina. From the proximal (top) to the distal (bottom) retina, alternate dark and light bands of signal in the OCT image directly correlate with the retinal layers, nerve fiber layer (NFL), ganglion cell layer (GCL), inner plexiform layer (IPL), inner nuclear layer (INL), and outer plexiform layer (OPL). Distal to a band attributable to the outer nuclear layer (ONL), a more delicate bright ribbon is likely to represent both the external limiting membrane and the myoid portion of the cone inner segments (IS). The adjacent dark and stippled signal is in alignment with the cone ellipsoids prominently seen using DIC optics. A distal dark band is possibly associated with the cone outer segment tips and, finally, the dark and light banding is attributable to the pigment epithelium–choriocapillaris complex. Scale bar-100 μm.

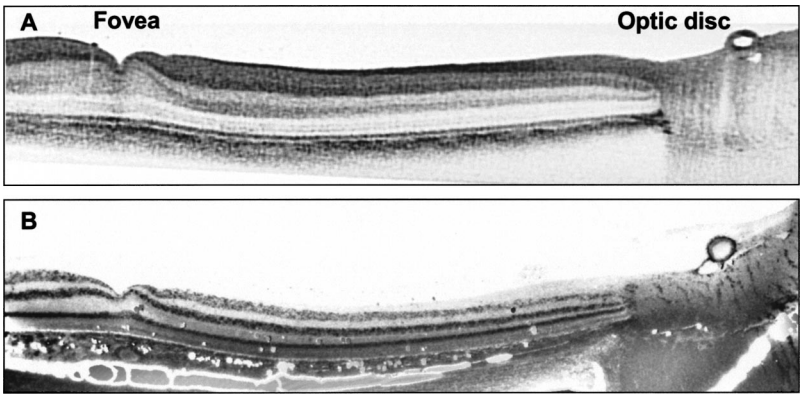

Fig. 13 Comparison of (a) *in vitro* ultrahigh-resolution OCT imaging (1×3 μm; axial×transverse) with (b) histology of a papillomacular section of a perfusion-fixed monkey (*Macaca fascicularis*) retina.

can be seen in acute CSC and partially in chronic CSC, whereas in AMD with minimal CNV, the PR layer and the ELM are affected by CNV in the center as well as the retinal and the retinal pigment epithelium detachment. In patients with AMD and vitelliform lesion, despite retinal detachment, the PR layer, the ELM, and the ONL appear quite normal, which explains the preservation of visual acuity in these patients.

Figure 16(a) depicts an ultrahigh-resolution OCT image of a healthy subject. Figure 16(b) shows the same foveal region of a 74-year-old patient with endstage glaucoma, documented by visual field [Fig. 16(c)] and a Heidelberg retinal tomogram image [Fig. 16(d)]. Compared with a scan acquired with ultrahigh resolution in a healthy subject, several morphological differences are obvious. Owing to increased intraocular pressure, the foveal depression is less pronounced in the endstage glaucoma patient (light gray arrows). Nasally there is no longer any thickness to the nerve fiber layer in this patient (white thick arrows). Finally, the ganglion cell layer is atrophied (circle with white thin arrows) and has a mean thickness of about 45 μm (together with the inner plexiform layer) in the parafoveal region, compared with about 100 μm in the normal subject. In addition to the distribution of the nerve fiber layer thickness around the optic disk, this atrophy of the ganglion cell layer in the foveal region might allow a novel approach for a more sensitive and specific early diagnosis of glaucoma.

Figure 17 demonstrates the potential of ophthalmic ultrahigh-resolution OCT to monitor and therefore contribute to a better understanding of novel therapeutic approaches. In this case the effect of an anti-vascular endothelium growth factor (VEGF) drug was investigated. This case was a 60-year-old woman with regressing drusen and placoid occult without classic choroidal neovascularization [Figs. 17(a) to 17(c)]. In addition to a normal appearance of the NFL, GCL, IPL, and INL, the photoreceptor layer is strongly compromised, owing to a serous detachment. Ultrahigh-resolution OCT makes it possible to visualize the occult membrane un-

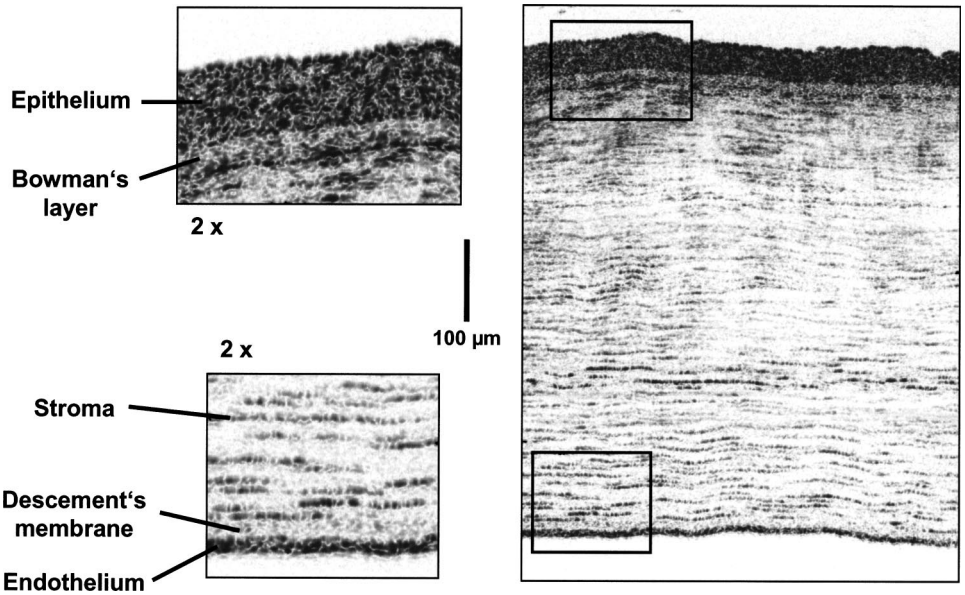

Fig. 14 *In vitro* ultrahigh-resolution OCT imaging (1×3 μm; axial×transverse) of a 4-day postmortem human cornea, visualizing all major intracorneal layers.

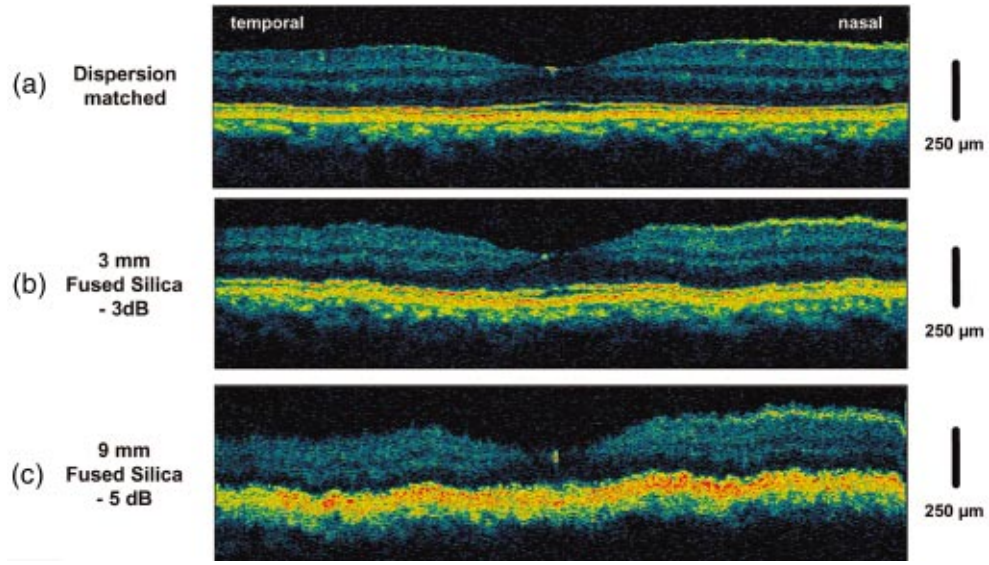

Fig. 6 Effect of dispersion mismatch in *in vivo* ultrahigh-resolution retinal imaging. (a) Dispersion matched. (b) Artificially introduced dispersion mismatch by 3 mm (middle) as well as (b) 9 mm of fused silica in the reference arm. Clear axial resolution as well as a degradation in sensitivity (up to −5 dB) is observed.

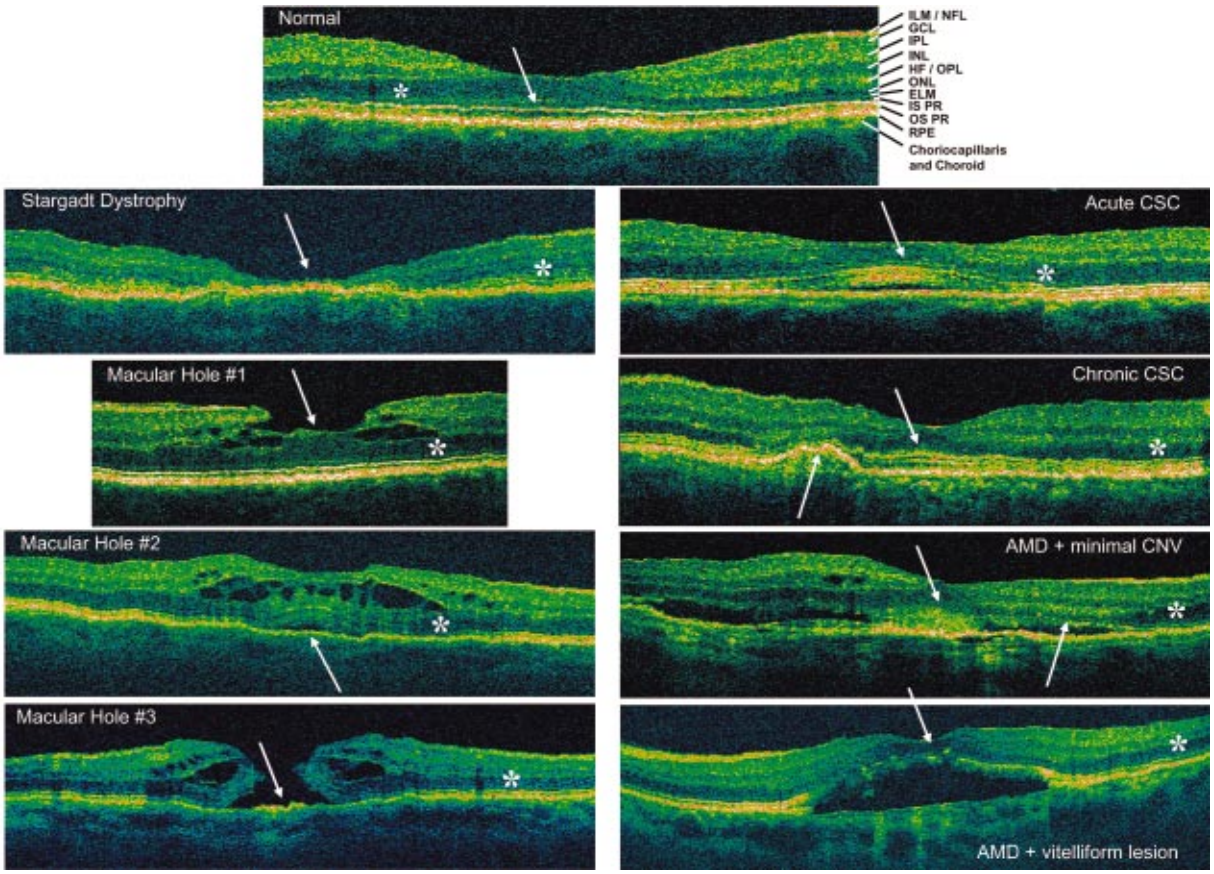

Fig. 15 *In vivo* ultrahigh-resolution OCT images of the foveal region of a normal human retina and different macular pathologies. The arrows indicate different appearances of the photoreceptor and outer nuclear layers, the asterisks indicate impairment of the external limiting membrane. ILM, internal limiting membrane; NFL, nerve fiber layer; GCL, ganglion cell layer; IPL, OPL, inner and outer plexiform layer; INL, ONL, inner and outer nuclear layer; HF, Henle's fiber layer; ELM, external limiting membrane; IS PR, inner segment of photoreceptor layer; OS PR, outer segment of photoreceptor layer; RPE, retinal pigment epithelium.

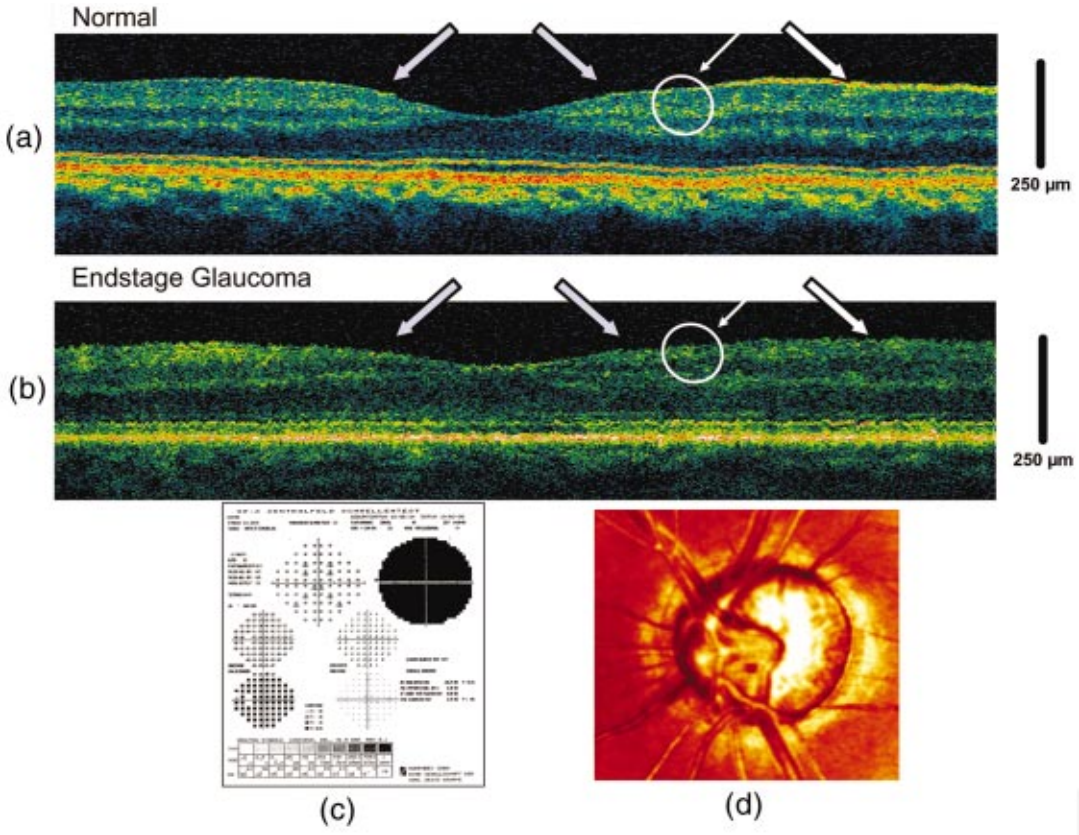

Fig. 16 *In vivo* ultrahigh-resolution OCT detecting and quantifying subtle changes for early diagnosis in (b) endstage glaucoma patient documented by visual field test (c) and (d) Heidelberg retinal tomogram (HRT) image compared with normal subjects (a). The gray arrows indicate the foveal pit contour and the white arrows indicate the lost nerve fiber layer. Atrophy in the ganglion cell and inner plexiform layer is shown by the circle and thin white arrows.

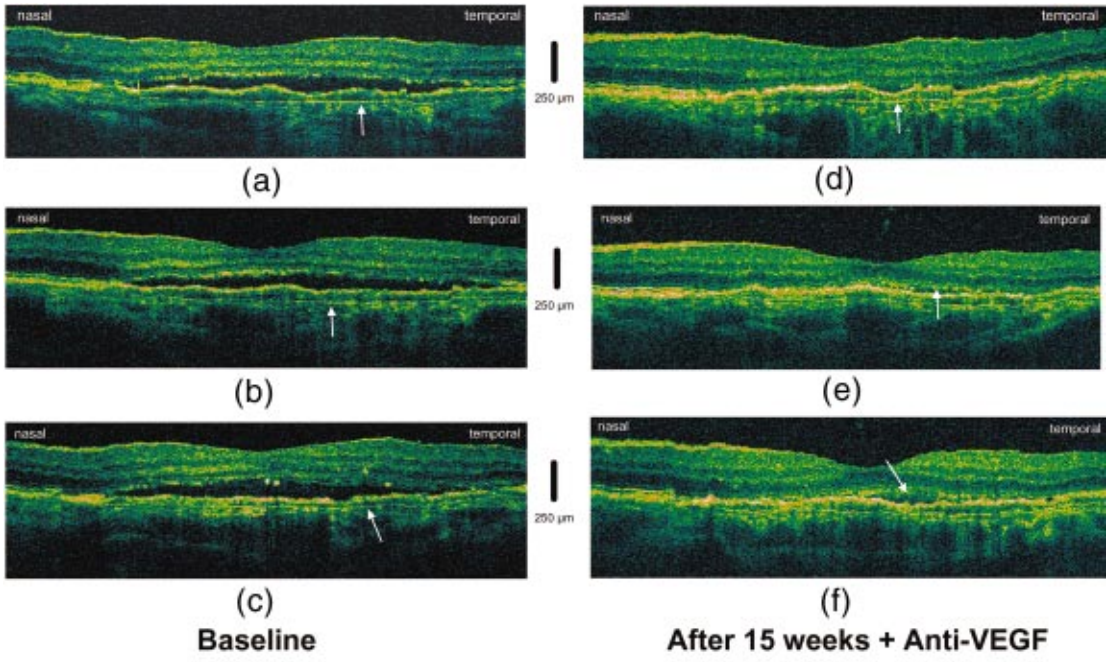

Fig. 17 Monitoring of new therapy approaches using *in vivo* ultrahigh-resolution OCT. A patient with regressing drusen with placoid occult without classic choroidal neovascularization before (a)–(c) and 15 weeks after treatment with anti-vascular endothelium growth factor (d)–(f).

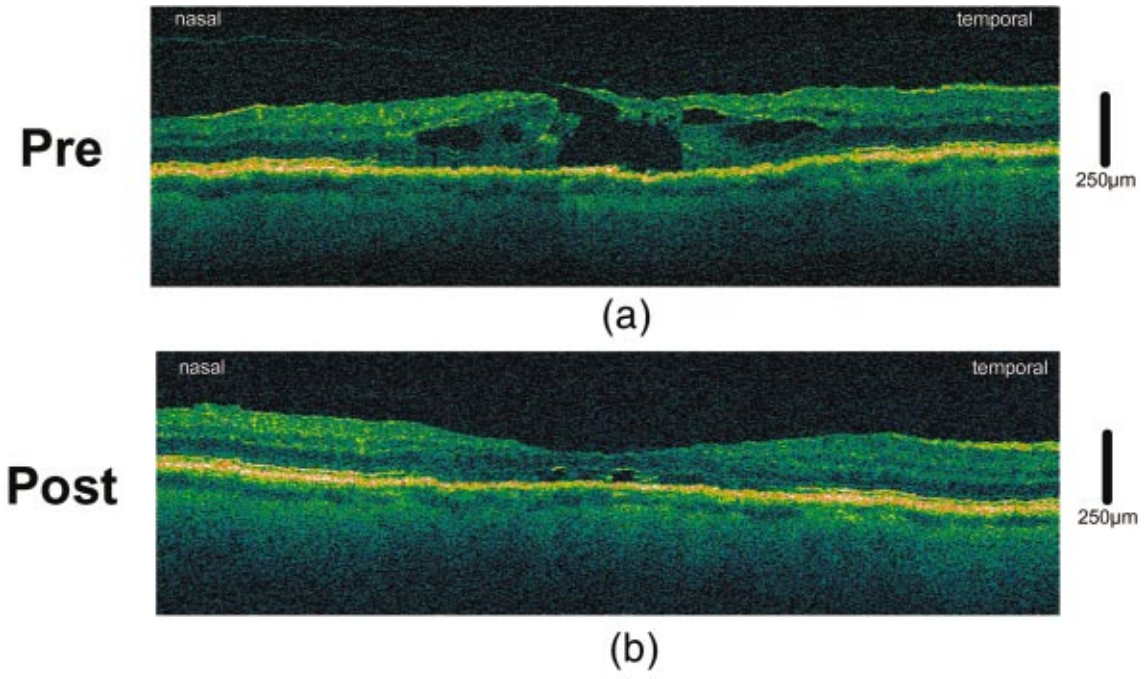

Fig. 18 Monitoring of surgical intervention with *in vivo* ultrahigh-resolution OCT. A patient with a macular hole is shown before (a) and after (b) surgery.

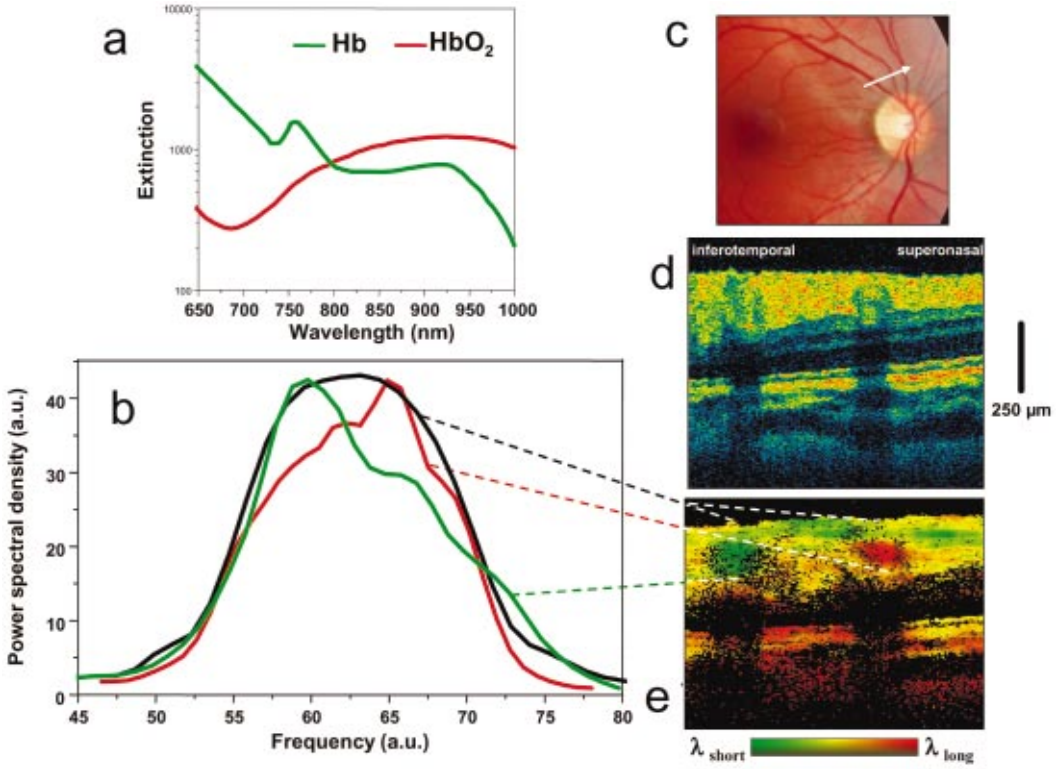

Fig. 28 *In vivo* spectroscopic OCT of the human retina. (a) Absorption characteristic of hemoglobin (Hb) and oxygenated hemoglobin (HbO_2) in the wavelength range used. (b) Spectra extracted after double passing a vein (green) and an artery (red) as well as the original spectrum of the light source (white); the spectra shown are an average over the indicated region (dashed lines). (c) Fundus photograph indicating the imaged site (arrow). (d) OCT amplitude. (e) Spectroscopic OCT image.

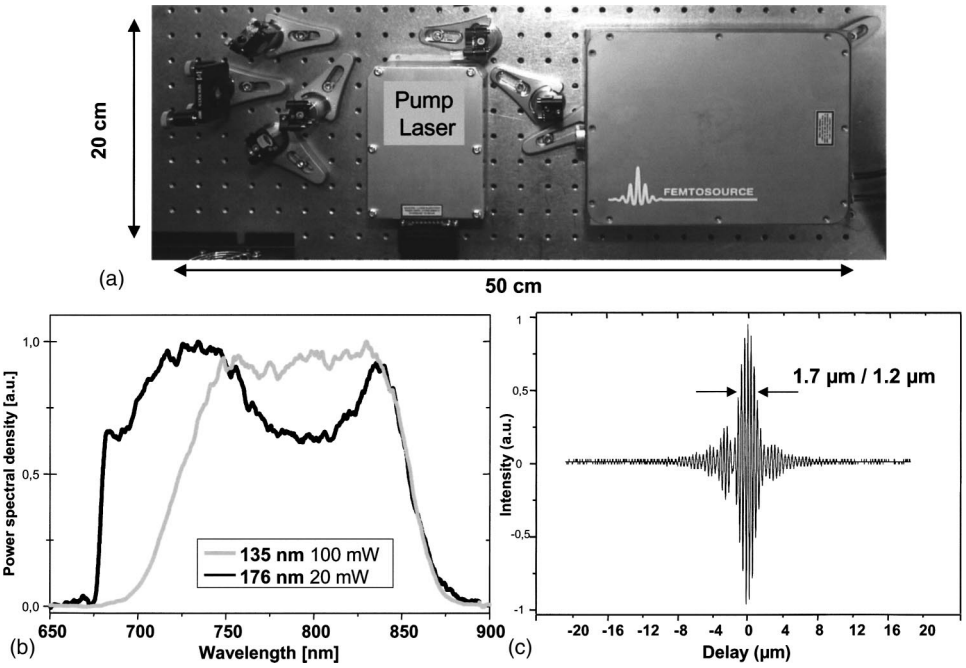

Fig. 19 Setup of the compact, low-cost Ti:sapphire laser. A commercially available compact (158×104 mm) 1.5-W source is used to pump a standard astigmatism-compensated X-folded cavity. (b) Typical optical output power spectra of this laser. (c) Interference signal (corresponding to the spectrum indicated with the solid black line, resulting in a free space axial resolution of 1.7 μm, corresponding to 1.2 μm in biological tissue).

derneath the RPE as well as the outer layer of Bruch's membrane, indicating intra-Bruch's choroidal neovascularization for the first time (arrows). In all three cross-sections, highly reflective particles in the outer photoreceptor layer, which could be isolated RP cells or damaged photoreceptors, could be differentiated by ultrahigh-resolution OCT. Fifteen weeks later, the effect of therapy treatment can clearly be visualized with ultrahigh-resolution ophthalmic OCT [Fig. 17(d) to 17(f)]. The PR complex has recovered but some subtle serous detachments as well as the occult membrane are still present. Finally, Fig. 18 demonstrates the potential of ophthalmic ultrahigh-resolution OCT to not only provide additional information about the status of the photoreceptor layer in patients with macular hole that can be used in a decision on surgical intervention, but it also may allow monitoring of the effect of this intervention and investigation of its outcome.

These preliminary results demonstrate that ultrahigh-resolution ophthalmic OCT enables unprecedented visualization of intraretinal morphology, which previously had been possible only with histopathology. It therefore provides a powerful tool for the clinical diagnosis of retinal diseases that are the leading causes of blindness. Furthermore, ultrahigh-resolution OCT provides a basic research and clinical tool for investigating the impairment of all major intraretinal layers, especially the photoreceptor layer associated with different macular pathologies. Its increased accuracy may allow the detection of intraretinal changes that can be used to diagnose retinal disease in its early stages, when treatment is most effective and irreversible damage can be prevented or delayed. Furthermore, it may provide a better understanding of the pathogenesis of several macular pathologies as well as the development of new therapeutic approaches.

The ultimate availability of this new technology for clinical research and patient care depends mainly on the availability of compact, reliable, low-cost lasers or other sources for ultrabroad-bandwidth light. Recently a compact, prismless, low-cost Ti:sapphire laser that employs a commercially available pump source has been used for *in vivo* ultrahigh-resolution imaging of macular pathologies.[139] It contains a standard astigmatism-compensated X-folded cavity with a compact low-cost 1.5-W pump source (158×104 mm) [Fig. 19(a)]. Dispersive mirrors are used to compensate for the second- and third-order dispersion of the laser crystal and air. Special broadband, low-loss dispersive mirrors were designed. The resonator is asymmetrically folded and some mirrors are used in double pass to reduce the laser size. The advantage of this prismless laser is that the design of the cavity is more compact and can act as a hands-off OCT laser source. The overall dimensions of the setup are 500 ×200 mm, including the pump laser. Kerr-lens mode locking is initiated by rapid translation of the end mirror, which is mounted on a translation stage to induce intensity fluctuations. The output power of the laser was strongly dependent on the bandwidth of the laser and varied from 100 mW with 135 nm to 20 mW with a 176-nm FWHM and a 70-MHz repetition rate [Fig. 19(b)]. For *ex vivo* OCT imaging, the broadest possible bandwidth [176 nm centered at 776 nm, see Fig. 19(b), black line] provided a peak axial resolution of 1.7 μm in free space, corresponding to about 1.2 μm in tissue [Fig. 19(c)].

This laser was interfaced to a fiber-based OCT system and achieved the same performance for axial resolution, sensitivity, and stability as a Ti:sapphire laser pumped by a 5-W

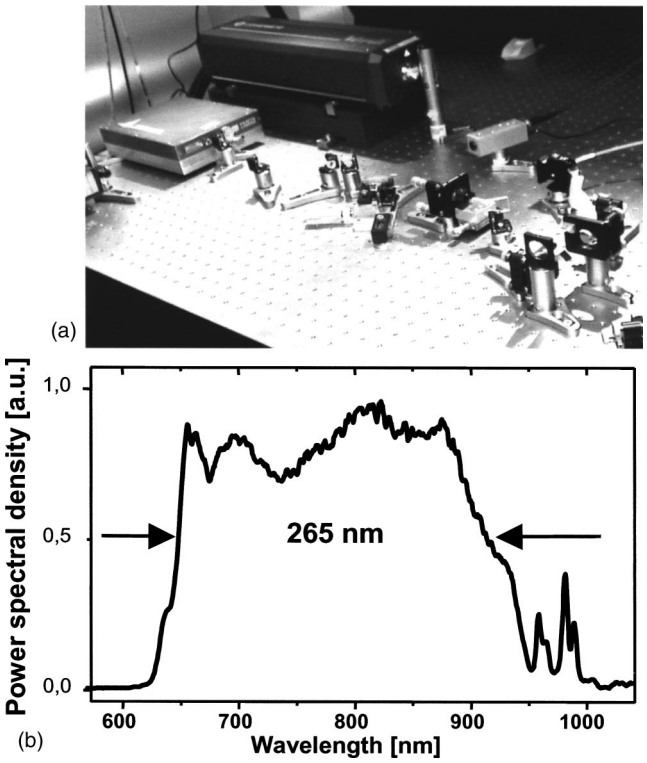

Fig. 20 (a) Setup of the compact, ultrabroad-bandwidth Ti:sapphire laser. (b) Typical optical output power spectra of this laser.

single-frequency, frequency-doubled, diode-pumped neodymium:vanadate laser.[139] For ultrahigh-resolution *in vivo* imaging in normal persons and patients, a less-modulated, Gaussianlike spectrum was used, compromising the bandwidth to 135 nm FWHM at 95 mW [Fig. 19(b), gray line] and obtaining an axial resolution in the retina of about 3 μm, which is similar to recent results. The system exhibits extremely reproducible spectra, output power, and user friendliness in day-to-day performance. Stable operation for more than 12 h with a 2% power loss and 2 to 5% loss in spectral bandwidth are usual.

An even further increase in the bandwidth using the same oscillator design can be achieved by replacing all high-reflecting mirrors by broadband dispersive mirrors and employing a single-frequency 532-nm pump source, which increases the footprint to 600×400 mm. The spectrum generated was 265 nm FWHM (Fig. 20). The bandwidth was only limited by the dichroic input coupler with an overall bandwidth of 300 nm. The average mode-locked output power is 250 mW with 3.65 W of pump power. This laser therefore has large potential to be used in combination with a low-cost pump laser and may be extremely interesting not only for *in vivo* submicrometer-resolution OCT, but also for functional, spectroscopic OCT.

4.2 *Ultrabroad-Bandwidth Light Sources in the 1300-nm Wavelength Region*

For OCT to be successfully used as an *in vivo* optical biopsy tool in nontransparent tissue, micrometer-scale resolution and millimeter-range penetration depth are required. In the range between 0.8 and 1.8 μm, scattering is the predominant mechanism limiting image penetration depth. Since scattering depends strongly on wavelength and decreases for longer wavelengths, a much higher image penetration depth in nontransparent tissue can be achieved with light at 1.35 μm than at 0.85 μm. It has been shown that the optimum wavelengths for imaging in nontransparent biological tissues are in the 1.3- to 1.5-μm range.[115,140] In this range, imaging depths of 2 to 3 mm can be achieved. Narrow-bandwidth superluminescent diodes or multiquantum well semiconductor amplifier used for OCT so far typically provide axial resolution of 10 to 20 μm. By multiplexing spectrally displaced light-emitting diodes (LEDs) at 1300 nm, a 7.2-μm axial resolution in free space could be obtained.[97]

In the 1300-nm wavelength region, ultrashort-pulse solid-state lasers are also promising light sources for ultrahigh-resolution OCT. In a first approach, a self-phase-modulated KLM chromium:forsterite (Cr:forsterite) laser has been used for *in vivo* OCT imaging in nontransparent tissues with 6-μm axial resolution.[74,141] Recent efforts were focused on developing even broader bandwidth light sources in the 1300-nm wavelength range that would permit OCT micrometer-scale resolution, along with millimeter-range penetration depth. A laser spectrum covering the 1230- to 1580-nm wavelength region with an optical bandwidth of 250 nm (FWHM) was generated directly out of an all-solid state Cr:forsterite laser.[142]

Spectra far broader than one optical octave can be produced via nonlinear propagation of laser pulses in microstructured fibers. Owing to the geometry of these fibers, the cross-section of the fundamental mode is unusually small, which enhances the peak power and thus the nonlinearity. At the same time, the fiber dispersion can be engineered to avoid fast temporal spreading. Owing to these effects, spectra covering more than one optical octave can be produced, even with pulses having moderated energies of a few nanojoules. This spectral width could never be generated directly from the laser oscillator because it exceeds the fluorescence bandwidth of the crystal. In order to avoid an excessively strong spectral modulation (inherent to the spectral broadening processes—self-phase modulation and four-wave mixing), only moderate spectral broadening should result from the nonlinear fiber propagation, i.e., the initial bandwidth of the pulses emerging from the oscillator should be as broad as possible. High nonlinearity, air-silica microstructure fibers,[143] or tapered fibers[144] have been used to generate an extremely broadband continuum using low-energy femtosecond pulses. In the latter approach, a standard single-mode fiber is heated and then lengthened. The light is initially guided inside the fiber core, but in the tapered region, the light propagates through the cladding. As in the air-hole fibers, the change in the index of refraction between the light-guiding region, the cladding in the tapered fibers, and the surrounding region, the air, is high. Depending on the cladding diameter, the zero-dispersion wavelength can be shifted. Both the air-hole fiber and the tapered fiber have been studied to find out optimum conditions for generating a broadband continuum with minimum noise.

So far, the highest reported OCT axial resolution in biological tissue in the 1300-nm wavelength region was obtained with the use of a complex laboratory prototype photoionic crystal fiber (PCF)-based light source.[145] With a bandwidth of

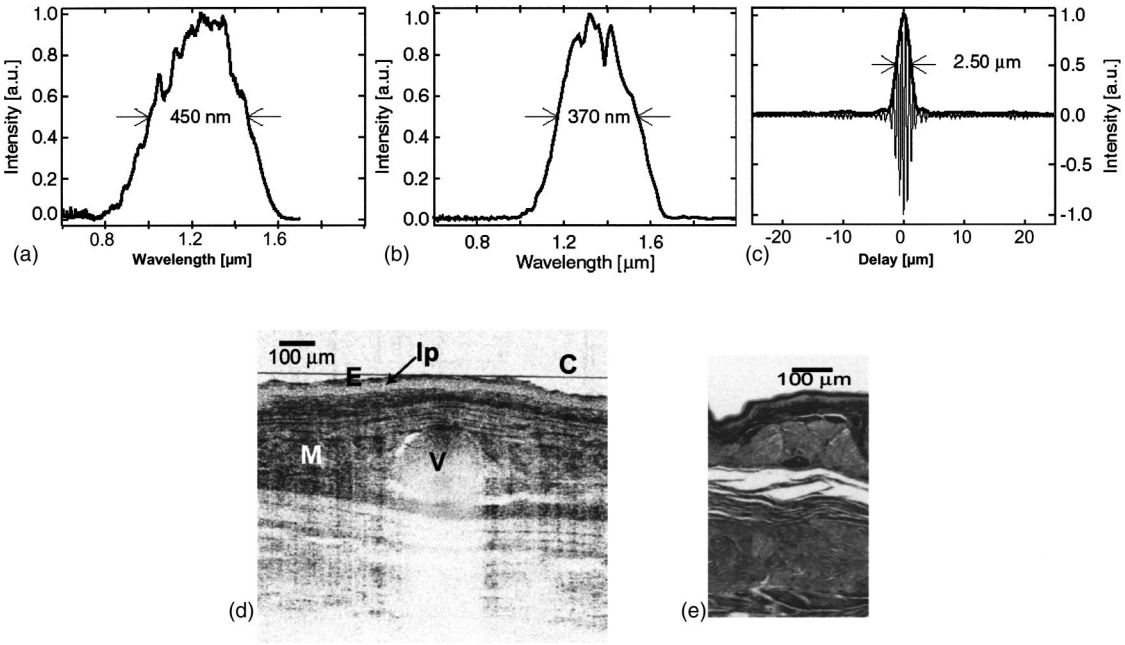

Fig. 21 Ti:sapphire-pumped PCF-based light source. With a bandwidth of 450 nm at a 1.3-μm center wavelength (a), 2.5 μm of axial resolution in free space (c), which corresponds to 2 μm in tissue, was achieved by employing an OCT system that could support a 370-nm bandwidth (b). *In vivo* ultrahigh-resolution imaging of a Syrian hamster's cheek pouch could be achieved. (d) Corresponding histology. (e) From Ref. 145 (with permission of Prof. J. G. Fujimoto, Cambridge, MA, USA).

450 nm at a 1.3-μm center wavelength [Figs. 21(a) and 21(b)], a 2.5-μm axial resolution in free space [Fig. 21(c)], which corresponds to 2 μm in tissue, was achieved by employing an OCT system that could support a 370-nm bandwidth [Fig. 21(c)]. Figure 21(d) depicts an *in vivo* ultrahigh-resolution image of a Syrian hamster's cheek pouch and Fig. 21(e) shows the corresponding histology. Recently, an unprecedented axial resolution of less than 2 μm in the 1300-nm wavelength range in nontransparent biological tissue was achieved with a novel, broad-bandwidth light source (MenloSystems), which due to its compactness, low cost, stability, and user friendliness offers a great potential for OCT clinical applications.[146] The MenloSystems light source is based on a pulsed erbium fiber laser, the amplified output of which is coupled into a highly nonlinear fiber to generate a supercontinuum ranging from 1100 to 1800 nm at its pedestal, with a power output of about 50 mW at a 50-MHz repetition rate. The light source is very compact ($145\times480\times300$ mm, corresponding to a 19-in. rack, 3 height units), low weight (8 kg), and has high mechanical stability. It provides a single mode fiber (SMF) 28 fiber-coupled output, which simplifies the interface to fiber optic OCT systems. Because of a 12-dB modulation at about 1550 nm, only the shorter wavelength portion of the emission spectrum was utilized for OCT imaging by blocking the wavelength range beyond 1550 nm with an edge filter. The filtered fiber laser spectrum was moderately modulated, centered at 1375 nm with a full width at half maximum of 470 nm and a power output of 4 mW (Fig. 22). By interfacing the MenloSystems light source to a free-space OCT system, a resolution of 2 μm in an axial, and 4 μm in a lateral direction (measured with a resolution target), corresponding to $\sim$1.4 μm and $\sim$3 μm in biological tissue, respectively (Fig. 22), and 95-dB sensitivity for 500-μW incident power were achieved.

The feasibility for an *ex vivo* sub-2-μm axial resolution OCT was demonstrated by imaging nonfixed human skin, arterial as well as gynecological biopsies (Fig. 22) demonstrating that the MenloSystems light source has great potential for applications in *in vivo* OCT clinical studies. Owing to its extremely broad output spectrum, this fiber laser-based light source also covers the 1550-nm wavelength region. Recent studies employing erbium- and thelium-doped fiber laser at 1.55 and 1.81 μm have demonstrated that these wavelength regions are interesting for OCT imaging of nontransparent tissue, because of good penetration depth despite the increased water absorption.[147] This might be due to the significantly reduced scattering in this wavelength region. Other broad-bandwidth light sources in this wavelength region that might be useful for OCT include a prismless 20-fs pulse Cr^{4+}: yttrium aluminum garnet (YAG) laser that offers a 190-nm bandwidth (FWHM) centered at 1400 nm with a 400-mW output power,[148] or an extremely powerful (2.4-W), ultrabroad-bandwidth (900-nm) compact white-light source that employs a passively mode-locked Nd:vanadate pump laser together with a dispersion-adapted air-silica microstructured fiber.[149]

4.3 *New Wavelength Regions for Ultrahigh Resolution OCT*

In the near-infrared region, a novel OCT light source might offer a unique opportunity to perform ophthalmic OCT imaging at 1100 nm, a spectral region where the transparency of ocular media is still good but the penetration below the retinal

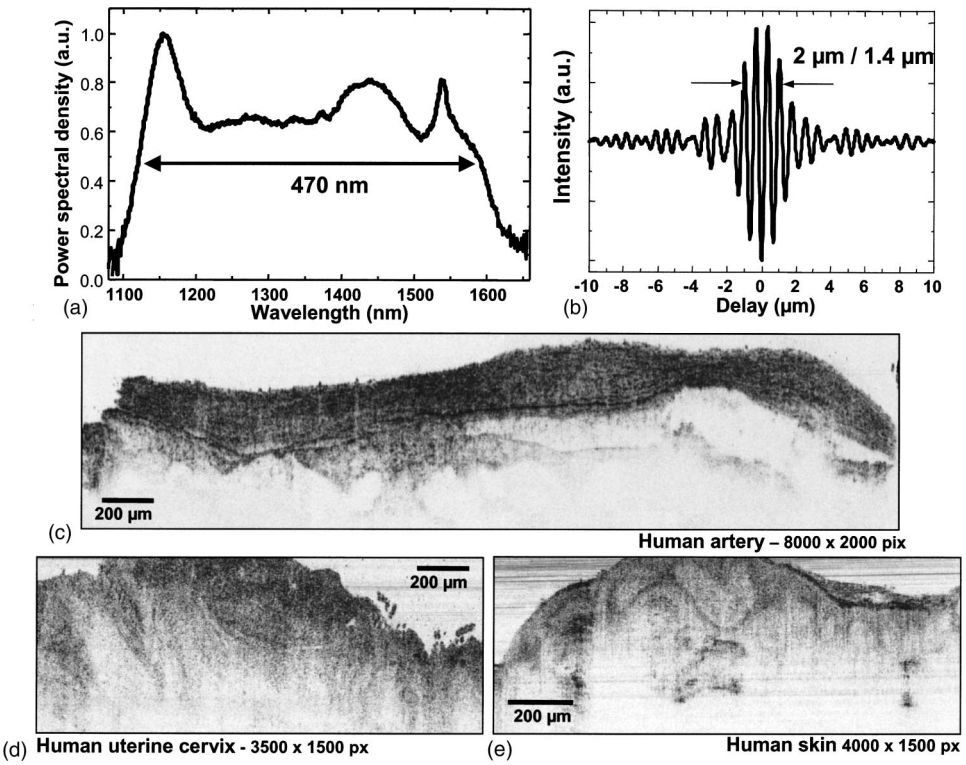

Fig. 22 (a) Typical optical output power spectra of a compact, ultrabroad-bandwidth fiber laser and (b) an interference signal corresponding to the spectrum that produces a free space axial resolution of 2 μm, corresponding to 1.4 μm in biological tissue. (c) to (e) *Ex vivo* ultrahigh-resolution OCT tomograms obtained with this light source.

pigment epithelium could be significantly enhanced. This might be very important not only for visualizing the choriocapillaris and choroid in the detection of diabetic macular edema but also for the detection of the angiogenesis process in age-related macular degeneration. Moreover, longer wavelengths should cause less attenuation in opaque eye media, which might occur in older patients as a result of cataract and haze in the cornea. Therefore, a photonic crystal fiber-based light source centered at about 1050 nm has recently been developed and was used to evaluate the image penetration depth of ultrahigh-resolution OCT in the choroid compared with a spectrally broadened fiber laser [$\lambda_c = 1350$ nm, $\Delta\lambda = 470$ nm, $P_{out} = 4$ mW; Figs. 23(a) and 23(b)] as well as a state-of-the art Ti:Al_2O_3 laser [$\lambda_c = 780$ nm, $\Delta\lambda = 160$ nm, $P_{out} = 400$ mW; Figs. 23(a) and 23(b)].[150] A PCF with a 1.9-μm core size and a 24-mm length was pumped with the output of a self-starting Ti:Al_2O_3 laser (FEMTO-LASERS; $\lambda_c = 790$ nm, $\Delta\lambda = 33$ nm, $P_{out} = 300$ mW; Fig. 23) to generate a broad-bandwidth spectrum, covering a local minimum in the water absorption spectrum located at about 1060 nm [Figs. 23(a) and 23(b)]. The PCF-generated supercontinuum, spanning 400 to 1200 nm, with $P_{out} = 60$ mW, was filtered with a long-pass filter to produce a spectrum ranging from 900 to 1200 nm with $P_{out} = 10$ mW. A free space resolution of 3.5 $\times 4$ μm (lateral$\times$axial), corresponding to 2.5$\times 3$ μm in tissue and 98 dB sensitivity at 2-mW of incident power was achieved by interfacing the PCF-based source to the OCT system.

The *ex vivo* pig retina tomogram [Fig. 23(c) 2000 $\times$1010 pixels, 2$\times$1 mm] acquired with the Ti:sapphire laser demonstrates that ultrahigh-resolution OCT in the 800-nm wavelength region permits detailed visualization of intraretinal layers. In comparison, the pig retina tomogram acquired with the PCF-based light source [Fig. 23(d), 2000 $\times$1010 pixels, 2$\times$1 mm] shows better penetration in the choroid (two layers of blood vessels are observed). Superior penetration in the choroid was achieved with the MenloSystems fiber laser, as demonstrated in the retinal tomogram in Fig. 23(e) (2000$\times$888 pixels, 2$\times$1 mm), where a group of interlaced vessels is clearly visible. This study demonstrated that with light sources centered at about 1050 and 1350 nm, the penetration depth of the OCT image in retinal tissue at longer wavelengths was superior. Compared with images acquired at about 800 nm, better visualization of the choriocapillary and choroid was achieved with the PCF-based source ($\sim$1050 nm). Superior penetration into the choroid was realized with the MenloSystems laser ($\sim$1350 nm), though owing to enhanced water absorption at longer wavelengths and the axial length of a human eye ($\sim$25 mm), this light source cannot be used for *in vivo* imaging of human retina. The fiber laser may find clinical applications for *in vivo* imaging of the anterior segment of a human eye. Furthermore, the fiber laser can be applied successfully in ophthalmic animal studies[13] since the eye length of a mouse is about 5 to 7 mm.

Spectra with up to 372 nm centered at about 1100 nm with about 50 mW of output power were recently generated by pumping a PCF with a 700-mW, 110-fs Ti:sapphire oscillator [Figs. 24(a) and 24(b)].[151] Nitrogen gas was used to avoid damage on the PCF fiber tip. An axial resolution of 1.8 μm was achieved [Figs. 24(c) and 24(d)] and *in vivo* ultrahigh-

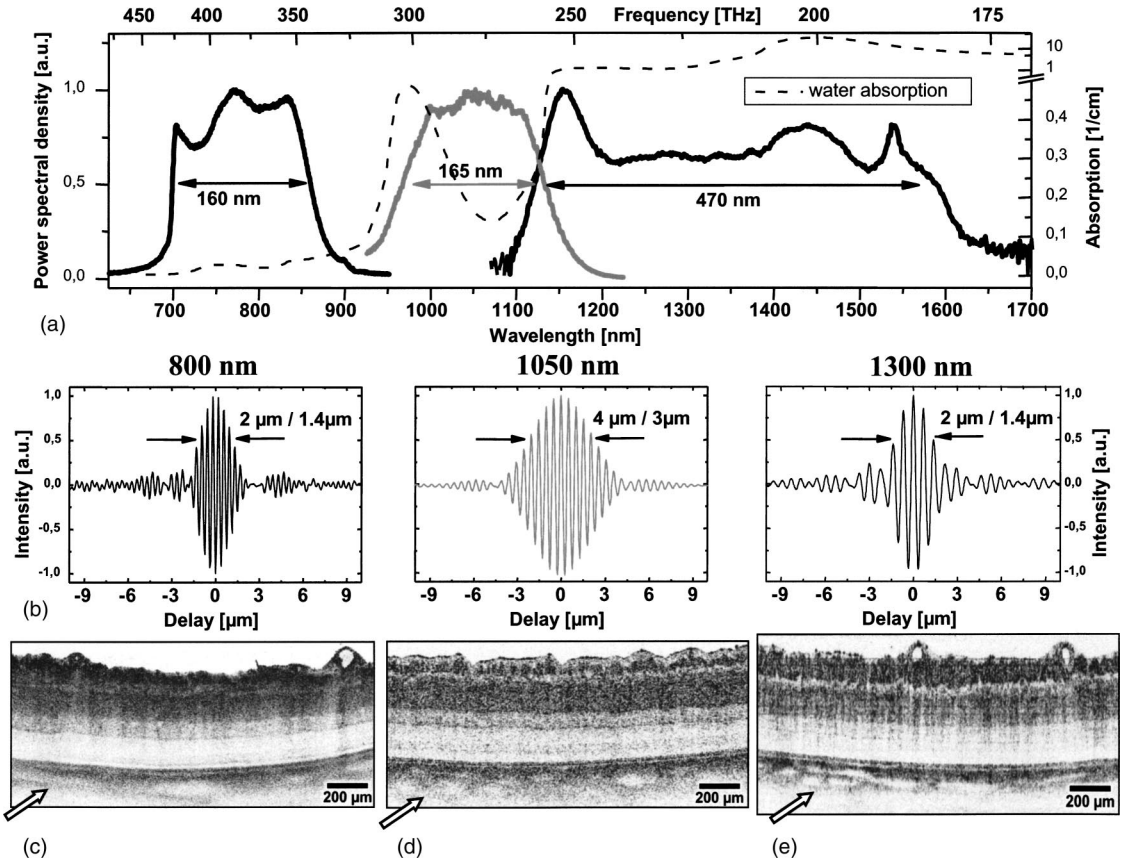

Fig. 23 (a) Output spectra of a Ti:sapphire (thin black line left), PCF-based source (gray line), and a MenloSystems laser (black line, right), overlaid with a water absorption spectrum (dashed line). (b) Corresponding fringe patterns produced by interfacing the light sources to the OCT system. (c) to (e) *Ex vivo* OCT images of pig retinas acquired with (c) the Ti:sapphire source (at about 800 nm, 2000×1000 pixels, 2×1 mm), (d) a PCF-based source (at about 1050 nm, 2000×1010 pixels, 2×1 mm), and (e) the fiber laser (at about 1350 nm, 2000×888 pixels, 2×1 mm) demonstrating enhanced penetration into the choroid with increasing wavelength.

resolution OCT imaging was demonstrated on an African tadpole (Xenopus laevis) [Figs. 24(e) to 24(f)]. This light source offers the broadest bandwidth ever achieved in the 1100-nm wavelength region. The disadvantage of ultrabroad-bandwidth spectra centered at 1100 nm is the lack of highly sensitive detectors for this wavelength region, since the spectrum covers a large portion of the detector sensitivity interface between silicon and indium-germanium-arsenic (InGaAs) detectors. Germanium or Si–InGaAs sandwiched detectors might be used, but are less sensitive than silicon and InGaAs detectors alone.

Recently, superluminescent diodes that cover a broad bandwidth in a similar wavelength region have become commercially available. These SLDs offer up to 70 nm of bandwidth (FWHM) centered at 950 nm with typically 3-mW ex fiber pigtail power as well as more than 100 nm of bandwidth (FWHM) centered at 900 nm with 3-mW free space output power. Unfortunately the output spectra of these light sources coincide with the water absorption peak around 980 nm. Therefore a portion of the output power will be absorbed and attenuated, especially in the case of ophthalmic OCT, where the beam has to propagate through 25 mm of ocular media consisting mainly of water.

For the first time, submicrometer OCT resolution has recently been achieved by using a PCF pumped with a compact, commercially available sub-10-fs Ti:sapphire laser. A stable, slightly modulated spectrum ranging from 550 to 950 nm (at its pedestal) with an output power of few tens of milliwatts was generated with this source, thus allowing in-depth imaging of biological tissue with unprecedented axial resolution.[152] The broad bandwidth of the light source also provides access to a spectral region covering the absorption bands of a number of biological chromophores; thus it has also great potential for spectroscopic OCT.

A 2.3-μm core diameter, 6-mm length PCF (University of Bath, UK) was pumped with a compact, commercially available Ti:sapphire (Al_2O_3) laser (Femtosource Compact Pro, FEMTOLASERS) emitting sub-10-fs pulses with about a 100-MHz repetition rate and an output power of up to 400 mW. By proper selection of the input pulse parameters and PCF characteristics, a spectrum spanning 325 nm, centered at 725 nm, with spectral modulations less than 1.5 dB and power output up to 27 mW was generated [Fig. 25(a)]. By interfacing the PCF source with a free space interferometer optimized to propagate the full bandwidth with minimum power and spectral losses and using a standard resolution chart, a free space OCT resolution of 2.5 μm in the lateral and 0.75 μm in the axial direction [corresponding to 0.5 μm in biological tissue; Fig. 25(b) has been achieved]. The axial resolution was

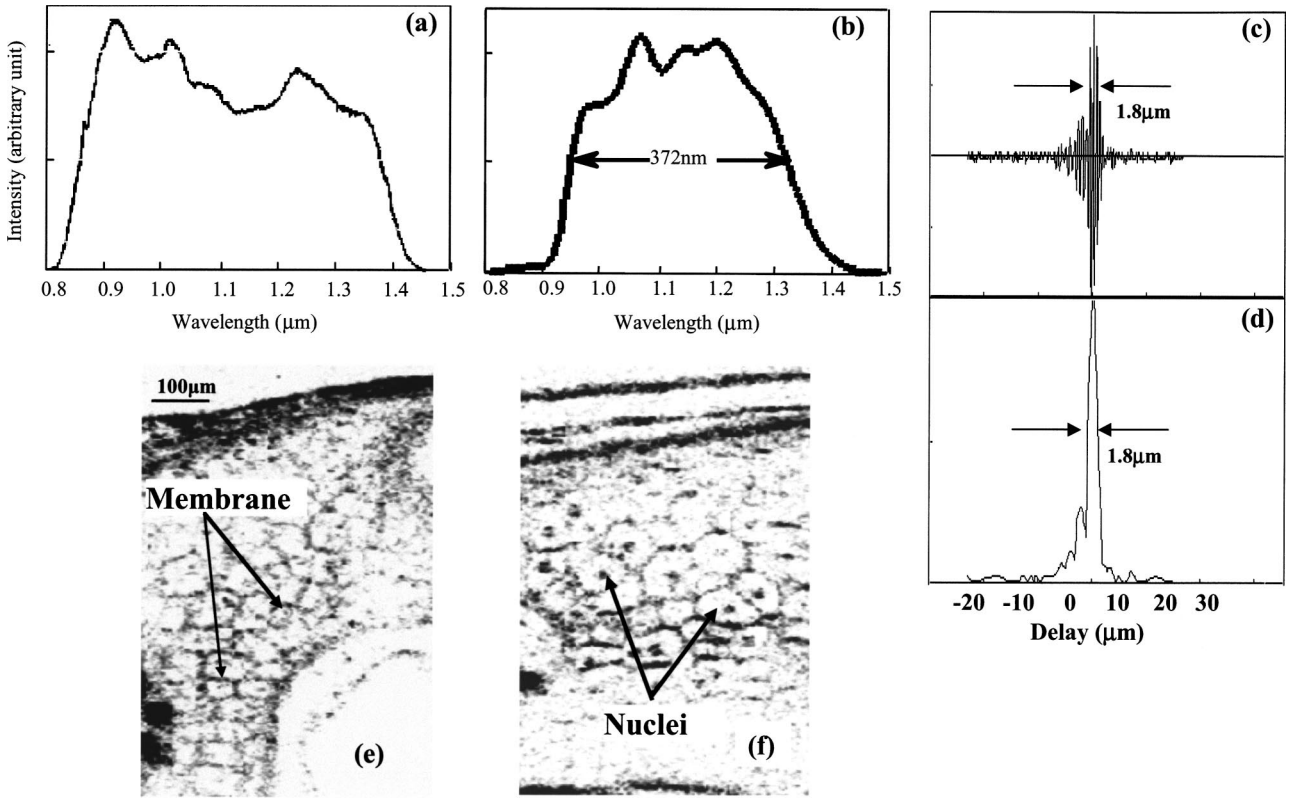

Fig. 24 (a) and (b) Spectra with up to 372 nm centered at about 1100 nm with about 50 mW of output power generated by pumping a PCF with a 700-mW, 110-fs Ti:sapphire oscillator achieving (c) and (d) 1.8-μm axial resolution. (e) and (f) *In vivo* ultrahigh-resolution OCT imaging on an African tadpole (*Xenopus laevis*) is depicted with (e) and without (f) dynamic focusing. (From Ref. 151.) (with the permission of Prof. Z. Chen, Beckman Laser Institute, University of California, Irvine, CA, USA)

defined as the FWHM of the envelope of the measured interferogram.

To demonstrate OCT in tissue with sub-micrometer axial resolution, human colorectal HT-29 adenocarcinoma cells were imaged *in vitro*. Multiple OCT cross-sectional images of a group of HT-29 cells were acquired *in vitro* with 0.5-μm axial and about 2-μm transverse resolution, covering an area of 50×50 μm (500×500 pixels) and equally spaced by 2 μm [Fig. 26(a)]. Histological sections of typical HT-29 cells parallel and perpendicular [Figs. 26(b) and 26(c)] to the OCT imaging direction are displayed for better interpretation of the OCT tomograms. A comparison with the histology shows that OCT images with a submicrometer resolution reveal features that may correspond to subcellular structures such as nucleoli that have a diameter of approximately 3 to 5 μm, as well as aggregates of cellular organelles.

5 Spectroscopic Optical Coherence Tomography

Spectroscopic and wavelength-dependent OCT is a new area of investigation and only few studies have been performed to

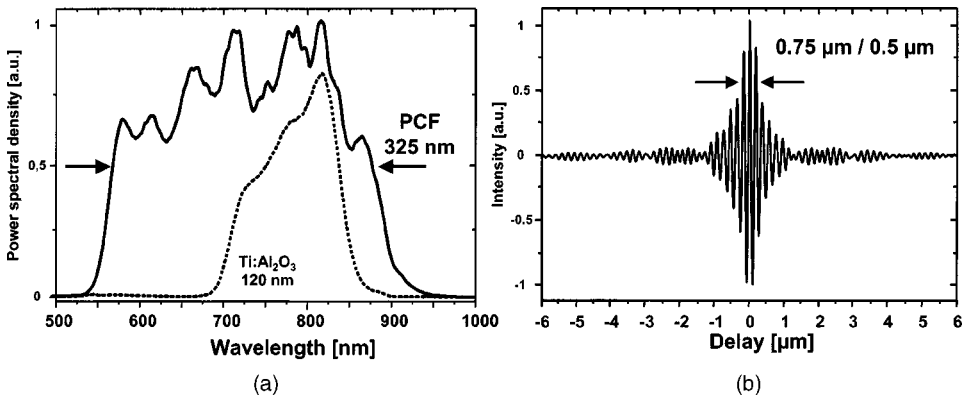

Fig. 25 (a) Optical spectrum of PCF output (solid line), PCF input spectrum (dashed line), and (b) corresponding interference signal.

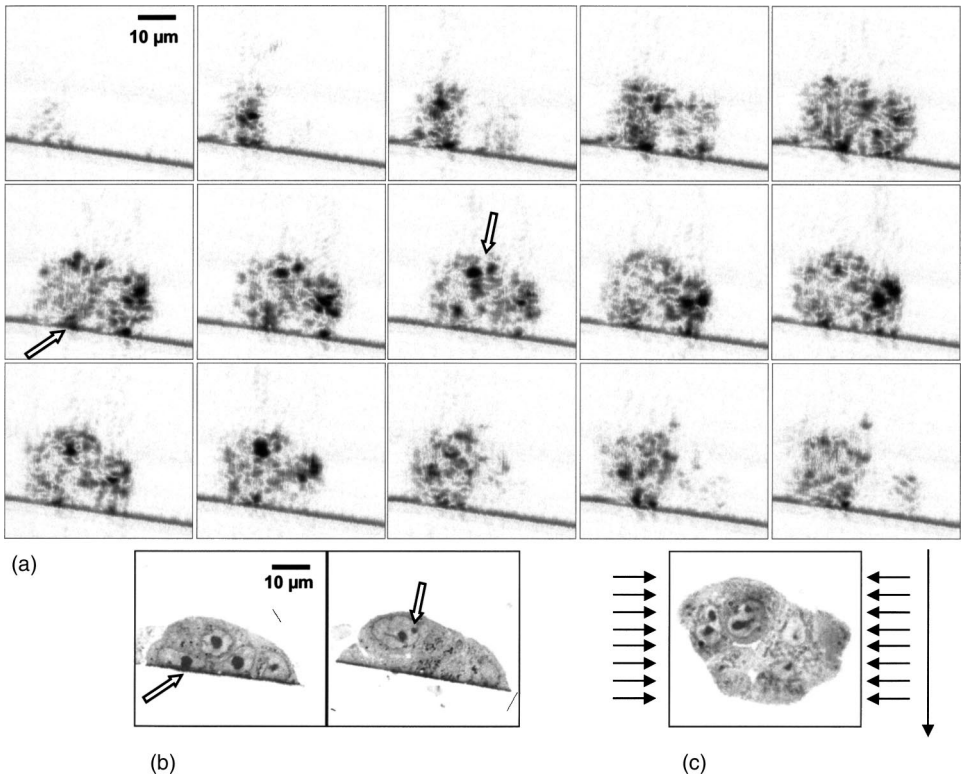

Fig. 26 (a) *In vitro* submicrometer-resolution OCT images of HT-29 human colorectal adenocarcinoma cells with 0.5-μm axial and about 2-μm transverse resolution, covering an area 50×50 μm, equally spaced by 2 μm. The arrows indicate features that may correspond to nucleoli with about a 3 to 5-μm diameter. Histological sections are shown parallel (b) and perpendicular (c) to the OCT imaging direction of typical HT-29 cells. [small black arrows in (c) indicate OCT imaging plane.]

date because sufficiently broad-bandwidth light sources have not been available.[153–155] Using state-of-the-art femtosecond Ti:sapphire lasers that emit broad-bandwidth light centered at 800 nm not only makes subcellular resolution possible for OCT but might also provide spectroscopic information over the entire output bandwidth. This spectral region is important because it overlaps with the so-called therapeutic window, covering absorption features of several biological chromophores.[156] Therefore this extended version of OCT might enable extraction of spatially resolved spectroscopic information to improve OCT image contrast via their spectroscopic properties and to obtain functional or biochemical information on the investigated tissue.

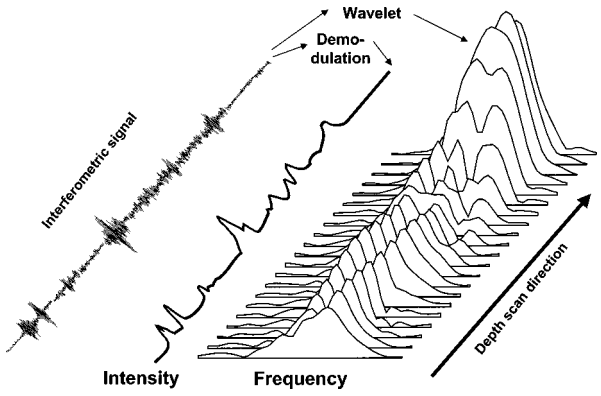

Fig. 27 Amplitude (intensity) versus spectroscopic imaging. Conventional OCT images are generated by using the envelope of the interferometer output. Optical spectroscopic information is mapped into the interference fringe frequency. Spectroscopic OCT is thus analogous to the classic technique of Fourier transform infrared spectroscopy. By using a windowed Fourier transform or wavelet transform, the spectrum of the backscattered light can be determined. Spectroscopic OCT requires broadband light sources, but has the advantage that the spectroscopic behavior at all wavelengths in the available bandwidth are characterized in a single measurement.

In standard OCT imaging, only the envelope of the interference signal is detected (Fig. 27). Spectral information can be obtained by measuring the full interference signal and using appropriate digital signal processing, e.g., using a Morlet-wavelet transform (Fig. 27). In order to display the spectroscopic data in a simple color image, the ''center of mass'' of the spectra were calculated in these preliminary experiments.[157] Spectroscopic OCT imaging requires a multidimensional map. This can be obtained by using hue, saturation, and luminance (HSL), color space (not RBG) and mapping the intensity into the saturation and the center of mass of the spectrum into the hue, keeping luminance constant. With all techniques that use reflected and backscattered light for imaging of tissue, the specific absorption and scattering properties of the intermediate tissues determine the amount of light that is detected from each location within the retina. In retinal vessels, red blood cells are the major component that contributes to absorption and scattering of the incident light. In addition, frequency changes in the backscattered light may be expected. The incident light scattered by moving erythrocytes is frequency shifted by the optical Doppler effect. This

frequency shift forms the basis of velocity measurements of retinal blood speed.

Figure 28(e) presents the same image as Fig. 28(d), but shows spectroscopic information. The retinal vessels can be easily identified, owing to the frequency shift (Δf) according to the optical Doppler effect. The retinal vein appears green whereas the retinal arteries appear red. This is due to differences in blood speed directions within the two vessels, as is expected when an artery and the adjacent vein are imaged. Another factor that affects the power spectrum is the difference in the hemoglobin and oxyhemoglobin extinction coefficients. With the broad spectrum obtained with Ti:sapphire-based OCT, it can be seen that behind the retinal vein the high-frequency spectrum of the power spectrum is blunted, whereas behind the retinal artery, the low-frequency spectrum is reduced [Figs. 28(a) and 28(b)]. This is due to the specific absorption characteristics within the two vessels, where oxyhemoglobin absorption predominates in the arteries (red) whereas hemoglobin absorption predominates in the veins (green) because of the large arteriovenous oxygen difference. In the retinal arteries, where the oxygen saturation is almost 100%, a convolution between the absorption curve of oxyhemoglobin and the incident power spectrum may be expected behind the retinal vessel.

It is important to note that OCT image contrast results from a combination of absorption and scattering. Incident light is attenuated by scattering and absorption as it propagates through the tissue, then is backscattered from the internal structure that is being imaged and is again attenuated as it propagates out of the tissue.[115] Thus the optical properties (absorption and scattering) of deep structures are convolved with the properties of the intervening structures, making it challenging to determine the exact optical properties of a given internal structure. However, OCT provides more information than other spectroscopic imaging techniques that integrate continuous wave backscattered light from multiple depths within tissue. Spectroscopic OCT may also be used to enhance image contrast, making it possible to differentiate tissue pathologies by their spectroscopic properties or functional state. Spectroscopic OCT could thus function as a type of ''spectroscopic staining,'' in analogy to staining in histopathology, and it should be able to detect spatially resolved functional and biochemical tissue information over the entire region of the emission wavelength of the light source with a single measurement.

6 Advantages and Benefit of Ultrahigh-Resolution OCT

This novel optical coherence tomography technology has been initiated and developed in collaboration with Prof. J. G. Fujimoto's laboratory at Massachusetts Institute of Technology, Cambridge, Massachusetts. It enables noninvasive *in vivo* optical biopsy for early diagnosis of neoplastic changes in different medical fields as well as early detection of ocular diseases. Ultrahigh-resolution OCT has the potential to provide real-time, *in situ* visualization of tissue microstructures without the need to excisionally remove and process a specimen as in conventional biopsy and histopathology. Nonexcisional optical biopsy and the ability to visualize tissue morphology *in vivo* at a subcellular resolution can be used both for diagnostic imaging and to guide therapeutic and surgical intervention. By improving the axial resolution by 2 orders of magnitude compared with conventional ultrasound, this technique represents a quantum leap in OCT imaging performance. In providing unprecedented noninvasive *in vivo* optical sectioning to visualize microscopic morphometric features with subcellular resolution in tissue at depths approaching those of *in vitro* conventional bright-field and confocal microscopes, this technique might dramatically enhance early cancer diagnosis as well as the early detection of a variety of ocular pathologies that are leading causes of blindness worldwide. In addition, an extension of this imaging technique has been developed that has the potential to provide spatially resolved functional imaging, i.e., spectroscopic as well as Doppler blood flow OCT. This extension should not only improve image contrast, but should also make it possible to differentiate tissue pathologies by localized spectroscopic properties or functional state.

This enhanced version of OCT will dramatically increase the diagnostic potential of *in vivo* OCT imaging technology since it will increase OCT resolution, increase the sensitivity of Doppler flow OCT, and give access to new wavelength ranges and spatially resolved spectrometric tissue properties. Hence, it is obvious that new morphological and functional information on pathological processes in tissue will become available. The hypothesis is that subcellular and intraretinal structures, which are relevant for the diagnosis and monitoring of early neoplastic changes as well as early eye diseases, can be seen by the proposed optical biopsy version of OCT and its extension for functional imaging. It is unlikely that OCT will replace excisional biopsy and histology or other existing diagnostic modalities. However, from the viewpoint of screening and diagnosis of diseases, the proposed version of OCT might lead to significant new insights in the pathogenesis and therapeutic control of several diseases. The unique features of this technology make it useful for a broad range of research and clinical applications, which might not only complement many of the imaging technologies available today, but also possibly reveal previously unseen morphological, dynamic, and functional changes in different biological tissues and medical fields.

Acknowledgments

The author would like to thank A. F. Fercher, head of the Department of Medical Physics, University of Vienna; J. G. Fujimoto, Massachusetts Institute of Technology, Cambridge, Massachusetts; H. Sattmann, B. Herrmann, A. Unterhuber, B. Povazay, K. Bizheva, and L. Schachinger, Department of Medical Physics, University of Vienna; F. Krausz, G. Tempea, V. Yakolev, and A. Apolonski, Photonics Institute, Technical University of Vienna; P. K. Ahnelt, C. Schubert, E. M. Anger, and M. Gloessmann, Department of Physiology, University of Vienna; A. Stingl, Ch. Warmuth, and A. Poppe, FEMTOLASERS Produktions GmbH, Vienna; M. Stur, C. Scholda, M. Wirtitsch, E. Ergun, and O. Findl, Department of Ophthalmology of the General Hospital of Vienna; M. Mei and R. Holzwarth, MenloSystems GmbH, Germany; W. J. Wadsworth, J. C. Knight, and Ph. St. J. Russell, Optoelectronics Group, Department of Physics, University of Bath, Bath, UK; J. E. Morgan and A. Cowey, University Hospital of Wales, Heath Park, Cardiff, Wales, UK; V. Wacheck, Department of

Clinical Pharmacology, General Hospital Vienna, Vienna University; H. Pehamberger, Department of Dermatology, General Hospital Vienna, Vienna University; M. Vetterlein and E. Scherzer, Institute of Histology and Embryology, University of Vienna; E. P. Ippen, F. X. Kärtner, R. K. Ghanta, T. H. Ko, and I. Hartl, Massachusetts Institute of Technology; U. Morgner, Universität Heidelberg, Germany; and J. S. Schuman, New England Eye Center, Tufts University School of Medicine, Boston, Massachusetts Support by Fonds zur Förderung der wissenschaftlischen Forschang (FWF) grants and P14218-PSY, Y 159, CRAF-1999-70549, the Christian Doppler Society, FEMTOLASERS Produktions GmbH, and Carl Zeiss Meditec Inc. is gratefully acknowledged.

Contributions from other groups (Prof. J. G. Fujimoto at MIT; Prof. Dr. C. Bocara and Dr. A. Dubois, Laboratoire d'Optique, Paris; and Prof. Z. Chen, Beckman Laser Institute, University of California, Irvine) are highly appreciated.

References

1. J. Ambrose and J. Hounsfield, ''Computerized transverse axial tomography,'' *Br. J. Radiol.* **46**, 148–149 (1972).
2. D. F. Chang, ''Ophthalmic examination,'' in *General Ophthalmology*, D. G. Vaughan, T. Asbury, and P. Rirodan-Eva, Eds., pp. 30–62, Appleton and Lange, Norwalk, CT (1992).
3. T. Seiler, ''Magnetic resonance imaging of the eye and orbit,'' in *Noninvasive Diagnostic Techniques in Ophthalmology*, B. R. Masters, Ed., pp. 17–31, Springer-Verlag, New York (1990).
4. A. W. Toga and J. C. Mazziotta, *Brain Mapping—The Methods*, Academic Press, New York (1996).
5. A. Villringer and U. Dirnagl, *Cerebrovasc Brain Metab. Rev.* **7**, 240–276 (1995).
6. S. Arridge, *Inverse Probl.* **15**, R41 (1999).
7. J. Powley, *Handbook of Biological Confocal Microscopy*, Plenum, New York (1995).
8. T. Olsen, ''The accuracy of ultrasonic determination of axial length in pseudophakic eyes,'' *Acta Ophthalmol.* **67**, 141–144 (1990).
9. J. C. Bamber and M. Trstam, ''Diagnostic ultrasound,'' in *The Physics of Medical Imaging*, S. Webb, Ed., pp. 319–388, Adam Hilger Bristol and Philadelphia, PA (1988).
10. J. C. Pavlin, J. A. McWhae, H. D. McGowan, and F. S. Foster, ''Ultrasound biomicroscopy of anterior segment tumors,'' *Ophthalmology* **99**, 1220–1228 (1992).
11. D. Z. Reinstein, R. H. Silverman, M. J. Rondeau, and D. J. Coleman, ''Epithelial and corneal thickness measurements by high-frequency ultrasound digital signal processing,'' *Ophthalmology* **101**(1), 140–146 (1994).
12. R. H. Webb, G. W. Hughes, and F. C. Delori, ''Flying spot TV ophthalmoscope,'' *Appl. Opt.* **19**, 2991–2997 (1979).
13. R. H. Webb, G. W. Hughes, and F. C. Delori, ''Confocal scanning laser ophthalmoscope,'' *Appl. Opt.* **26**, 1492–1499 (1987).
14. J. F. Bille, A. W. Dreher, and G. Zinser, ''Scanning laser tomography of the living human eye,'' in *Noninvasive Diagnostic Techniques in Ophthalmology*, B. R. Master, Ed., pp. 528–547, Springer-Verlag, New York (1990).
15. B. R. Masters and A. A. Thaer, ''Real-time scanning slit confocal microscopy of the *in vivo* human cornea,'' *Appl. Opt.* **33**(4), 695–701 (1994).
16. B. R. Masters, ''Three-dimensional confocal microscopy of the living *in situ* rabbit cornea,'' *Opt. Express* **3**(9), 351–355 (1998).
17. R. C. Youngquist, S. Carr, and D. E. N. Davies, ''Optical coherence domain reflectometry: a new optical evaluation technique,'' *Opt. Lett.* **12**, 158–160 (1987).
18. K. Takada, I. Yokohama, K. Chida, and J. Noda, ''New measurement system for fault location in optic waveguide devices based on an interferometric technique,'' *Appl. Opt.* **26**, 1603 (1987).
19. A. F. Fercher and E. Roth, ''Ophthalmic laser interferometer,'' *Proc. SPIE* **658**, 48–51 (1986).
20. J. G. Fujimoto, S. De Silvestri, E. P. Ippen, C. A. Puliafito, R. Margolis, and A. Oseroff, ''Femtosecond optical ranging in biological systems,'' *Opt. Lett.* **11**, 150–152 (1986).
21. A. F. Fercher, K. Mengedoht, and W. Werner, ''Eye length measurement by interferometer with partially coherent light,'' *Opt. Lett.* **13**, 186–188 (1988).
22. D. Huang, E. A. Swanson, C. P. Lin et al., ''Optical coherence tomography,'' *Science* **254**, 1178–1181 (1991).
23. D. Huang, J. Wang, C. P. Lin, C. A. Puliafito, and J. G. Fujimoto, ''Micron-resolution ranging of cornea anterior chamber by optical reflectometry,'' *Lasers Surg. Med.* **11**, 419–425 (1991).
24. A. F. Fercher, ''Optical coherence tomography,'' *J. Biomed. Opt.* **1**, 157–173 (1996).
25. C. K. Hitzenberger, ''Optical measurement of the axial eye length by laser Doppler interferometer,'' *Invest. Ophthalmol. Visual Sci.* **32**, 616–624 (1991).
26. C. K. Hitzenberger, W. Drexler, C. Dolezal, F. Skorpik, M. Juchem, A. F. Fercher, and H. D. Gnad, ''Measurement of the axial length of cataract eyes by laser Doppler interferometry,'' *Invest. Ophthalmol. Visual Sci.* **34**, 1886–1893 (1993).
27. C. K. Hitzenberger, W. Drexler, and A. F. Fercher, ''Measurement of corneal thickness by laser Doppler interferometry,'' *Invest. Ophthalmol. Visual Sci.* **33**, 98–103 (1992).
28. C. K. Hitzenberger, A. Baumgartner, W. Drexler, and A. F. Fercher, ''Interferometric measurement of corneal thickness with micrometer precision,'' *Am. J. Ophthalmol.* **118**(4), 468–476 (1994).
29. W. Drexler, C. K. Hitzenberger, H. Sattmann, and A. F. Fercher, ''Measurement of the thickness of fundus layers by partial coherence tomography,'' *Opt. Eng.* **34**(3), 701–710 (1995).
30. W. Drexler, A. Baumgartner, O. Findl, C. K. Hitzenberger, H. Sattmann, and A. F. Fercher, ''(Sub)micrometer precision biometry of the anterior segment of the human eye,'' *Invest. Ophthalmol. Visual Sci.* **38**(7), 1304–1313 (1997).
31. M. Wirtitsch, O. Findl, R. Menapace, V. Petternell, B. Kiss, C. K. Hitzenberger, A. F. Fercher, and W. Drexler, ''Effect of dorzolamide on corneal thickness in humans with low endothelial cell count,'' *Arch. Ophthalmol. (Chicago)* **121**, 621–625 (2003).
32. O. Findl, W. Drexler, R. Menapace, C. K. Hitzenberger, and A. F. Fercher, ''High precision biometry of pseudophakic eyes using partial coherence interferometry,'' *J. Cataract Refractive Surg.* **24**(8), 1087–1093 (1998).
33. O. Findl, W. Drexler, R. Menapace, B. Bobr, S. Bittermann, C. Vass, G. Rainer, C. K. Hitzenberger, and A. F. Fercher, ''Accurate determination of effective lens position and lens-capsule distance with 4 intraocular lenses,'' *J. Cataract Refractive Surg.* **24**(8), 1094–1098 (1998).
34. V. Petternel, C. M. Köppl, I. Dejaco-Ruhswurm, O. Findl, C. Skorpik, and W. Drexler (corresponding author), ''Effect of accommodation and pupil size on the movement of a posterior chamber lens in the phakic eye,'' *Ophthalmology* (in press).
35. W. Drexler, A. Baumgartner, C. K. Hitzenberger, O. Findl, and A. F. Fercher, ''Biometric investigation of changes in the anterior eye segment during accommodation,'' *Vision Res.* **37**(19), 2789–2800 (1997).
36. O. Findl, R. Menapace, B. Kiss, V. Petternell, M. Georgopoulos, G. Rainer, and W. Drexler, ''IOL movement induced by ciliary muscle contraction,'' *J. Cataract Refractive Surg.* **29**(4), 669–676 (2003).
37. W. Drexler, O. Findl, L. Schmetterer, C. K. Hitzenberger, and A. F. Fercher, ''Eye elongation during accommodation in humans—differences between emmetropes and myopes,'' *Invest. Ophthalmol. Visual Sci.* **39**(11), 2140–2147 (1998).
38. W. Drexler, O. Findl, R. Menapace, G. Rainer, C. Vass, C. K. Hitzenberger, and A. F. Fercher, ''Partial coherence interferometry: a novel approach to biometry in cataract surgery,'' *Am. J. Ophthalmol.* **126**(4), 524–534 (1998).
39. O. Findl, W. Drexler, R. Menapace, H. Heinzl, C. K. Hitzenberger, and A. F. Fercher, ''Improved prediction of intraocular lens power using partial coherence interferometry,'' *J. Cataract Refractive Surg.* **27**(6), 861–867 (2001).
40. O. Findl, W. Drexler, R. Menapace, B. Kiss, C. K. Hitzenberger, and A. F. Fercher, ''Optical biometry in cataract surgery,'' *Dev. Neurosci.* **34**, 131–140 (2002).
41. W. Drexler, C. K. Hitzenberger, A. Baumgartner, O. Findl, H. Sattmann, and A. F. Fercher, ''Investigation of dispersion effects in ocular media by multiple wavelength partial coherence interferometry,'' *Exp. Eye Res.* **66**, 25–33 (1997).
42. A. F. Fercher, C. K. Hitzenberger, W. Drexler, G. Kamp, and H. Sattmann, ''*In vivo* optical coherence tomography,'' *Am. J. Ophthalmol.* **116**, 113–114 (1993).

43. W. Drexler, O. Findl, R. Menapace, A. Wedrich, A. Kruger, G. Rainer, A. Baumgartner, C. K. Hitzenberger, and A. F. Fercher, ''Dual beam optical coherence tomography: signal identification for ophthalmologic diagnosis,'' *J. Biomed. Opt.* **3**(1), 55–65 (1998).
44. E. A. Swanson, D. Huang, M. R. Hee, J. G. Fujimoto, C. P. Lin, and C. A. Puliafito, ''High-speed optical coherence reflectometry,'' *Opt. Lett.* **17**(2), 151–153 (1992).
45. E. A. Swanson, J. A. Izatt, M. R. Hee, D. Huang, C. P. Lin, J. S. Schuman, C. A. Puliafito, and J. G. Fujimoto, ''*In vivo* retinal imaging by optical coherence tomography,'' *Opt. Lett.* **18**(21), 1864–1866 (1993).
46. C. A. Puliafito, M. R. Hee, J. S. Schuman, and J. G. Fujimoto, ''Optical coherence tomography of ocular disease,'' Slack Inc., Thorofare, NJ (1995).
47. J. A. Izatt, M. R. Hee, E. A. Swanson, C. P. Lin, D. Huang, J. S. Schuman, C. A. Puliafito, and J. G. Fujimoto, ''Micrometer-scale resolution imaging of the anterior eye *in vivo* with optical coherence tomography,'' *Arch. Ophthalmol.* **112**(12), 1584–1589 (1994).
48. S. Radhakrishnan, A. M. Rollins, J. E. Roth, S. Yazdanfar, V. Westphal, D. S. Bardenstein, and J. A. Izatt, ''Real-time optical coherence tomography of the anterior segment at 1310 nm,'' *Arch. Ophthalmol.* **119**(8), 1179–1185 (2001).
49. M. R. Hee, J. A. Izatt, E. A. Swanson, J. S. Schuman, C. P. Lin, C. A. Puliafito, and J. G. Fujimoto, ''Optical coherence tomography of the human retina,'' *Arch. Ophthalmol.* **113**, 325–332 (1995).
50. C. A. Puliafito, M. R. Hee, C. P. Lin, E. Reichel, J. S. Schuman, J. S. Duker, J. A. Izatt, E. A. Swanson, and J. G. Fujimoto, ''Imaging of macular diseases with optical coherence tomography,'' *Ophthalmology* **102**, 217–229 (1995).
51. M. R. Hee, C. A. Puliafito, C. Wong, J. S. Duker, B. Rutledge, J. S. Schuman, E. A. Swanson, and J. G. Fujimoto, ''Quantitative assessment of macular edema with optical coherence tomography,'' *Arch. Ophthalmol.* **113**(8), 1019–1029 (1995).
52. M. R. Hee, C. A. Puliafito, J. S. Duker, E. Reichel, J. G. Coker, J. R. Wilkins, J. S. Schuman, E. A. Swanson, and J. G. Fujimoto, ''Topography of diabetic macular edema with optical coherence tomography,'' *Ophthalmology* **105**(2), 360–370 (1998).
53. M. R. Hee, C. A. Puliafito, C. Wong, J. S. Duker, E. Reichel, J. S. Schuman, E. A. Swanson, and J. G. Fujimoto, ''Optical coherence tomography of macular holes,'' *Ophthalmology* **102**(5), 748–756 (1995).
54. M. R. Hee, C. A. Puliafito, C. Wong, E. Reichel, J. S. Duker, J. S. Schuman, E. A. Swanson, and J. G. Fujimoto, ''Optical coherence tomography of central serous chorioretinopathy,'' *Am. J. Ophthalmol.* **120**(1), 65–74 (1995).
55. M. R. Hee, C. R. Baumal, C. A. Puliafito, J. S. Duker, E. Reichel, J. R. Wilkins, J. G. Coker, J. S. Schuman, E. A. Swanson, and J. G. Fujimoto, ''Optical coherence tomography of age-related macular degeneration and choroidal neovascularization,'' *Ophthalmology* **103**(8), 1260–1270 (1996).
56. J. R. Wilkins, C. A. Puliafito, M. R. Hee, J. S. Duker, E. Reichel, J. G. Coker, J. S. Schuman, E. A. Swanson, and J. G. Fujimoto, ''Characterization of epiretinal membranes using optical coherence tomography,'' *Ophthalmology* **103**(12), 2142–2151 (1996).
57. J. S. Schuman, M. R. Hee, C. A. Puliafito, C. Wong, T. Pedut-Kloizman, C. P. Lin, E. Hertzmark, J. A. Izatt, E. A. Swanson, and J. G. Fujimoto, ''Quantification of nerve fiber layer thickness in normal and glaucomatous eyes using optical coherence tomography,'' *Arch. Ophthalmol.* **113**, 586–596 (1995).
58. J. S. Schuman, T. Pedut-Kloizman, E. Hertzmark, M. R. Hee, J. R. Wilkins, J. G. Coker, C. A. Puliafito, J. G. Fujimoto, and E. A. Swanson, ''Reproducibility of nerve fiber layer thickness measurements using optical coherence tomography,'' *Ophthalmology* **103**(11), 1889–1898 (1996).
59. R. F. Spaide, ''Macular hole repair with minimal vitrectomy,'' *Retina* **22**(2), 183–186 (2002).
60. S. Muscat, S. Parks, E. Kemp, and D. Keating, ''Repeatability and reproducibility of macular thickness measurements with the Humphrey OCT system,'' *Invest. Ophthalmol. Visual Sci.* **43**(2), 490–495 (2002).
61. R. F. Spaide, D. Wong, Y. Fisher, and M. Goldbaum, ''Correlation of vitreous attachment and foveal deformation in early macular hole states,'' *Am. J. Ophthalmol.* **133**(2), 226–229 (2002).
62. C. Bowd, L. M. Zangwill, E. Z. Blumenthal et al., ''Imaging of the optic disc and retinal nerve fiber layer: the effects of age, optic disc area, refractive error, and gender,'' *J. Opt. Soc. Am. A* **19**(1), 197–207 (2002).
63. P. Massin, B. Haouchine, and A. Gaudric, ''Macular traction detachment and diabetic edema associated with posterior hyaloidal traction,'' *Am. J. Ophthalmol.* **132**(4), 599–600 (2001).
64. C. Sanchez-Galeana, C. Bowd, E. Z. Blumenthal, P. A. Gokhale, L. M. Zangwill, and R. N. Weinreb, ''Using optical imaging summary data to detect glaucoma,'' *Ophthalmology* **108**(10), 1812–1818 (2001).
65. C. Bowd, L. M. Zangwill, C. C. Berry et al., ''Detecting early glaucoma by assessment of retinal nerve fiber layer thickness and visual function,'' *Invest. Ophthalmol. Visual Sci.* **42**(9), 1993–2003 (2001).
66. P. Massin, C. Allouch, B. Haouchine et al., ''Optical coherence tomography of idiopathic macular epiretinal membranes before and after surgery,'' *Am. J. Ophthalmol.* **130**(6), 732–739 (2000).
67. M. E. Pons, H. Ishikawa, R. Gurses-Ozden, J. M. Liebmann, H. L. Dou, and R. Ritch, ''Assessment of retinal nerve fiber layer internal reflectivity in eyes with and without glaucoma using optical coherence tomography,'' *Arch. Ophthalmol.* **118**(8), 1044–1047 (2000).
68. D. S. Chauhan, R. J. Antcliff, P. A. Rai, T. H. Williamson, and J. Marshall, ''Papillofoveal traction in macular hole formation: the role of optical coherence tomography,'' *Arch. Ophthalmol.* **118**(1), 32–38 (2000).
69. A. Gaudric, B. Haouchine, P. Massin, M. Paques, P. Blain, and A. Erginay, ''Macular hole formation: new data provided by optical coherence tomography,'' *Arch. Ophthalmol.* **117**(6), 744–751 (1999).
70. R. Brancato, ''Optical coherence tomography (OCT) in macular edema,'' *Doc. Ophthalmol.* **97**(3–4), 337–339 (1999).
71. J. G. Fujimoto, M. E. Brezinski, G. J. Tearney, S. A. Boppart, B. E. Bouma, M. R. Hee, J. F. Southern, and E. A. Swanson, ''Optical biopsy and imaging using optical coherence tomography,'' *Nat. Med.* **1**, 970–972 (1995).
72. M. E. Brezinski, G. J. Tearney, B. E. Bouma, S. A. Boppart, M. R. Hee, E. A. Swanson, J. F. Southern, and J. G. Fujimoto, ''Imaging of coronary artery microstructure (*in vitro*) with optical coherence tomography,'' *Am. J. Cardiol.* **77**(1), 92–93 (1996).
73. J. G. Fujimoto, B. Bouma, G. J. Tearney, S. A. Boppart, C. Pitris, J. F. Southern, and M. E. Brezinski, ''New technology for high-speed and high-resolution optical coherence tomography,'' *Ann. N.Y. Acad. Sci.* **838**, 95–107 (1998).
74. S. A. Boppart, B. E. Bouma, C. Pitris, J. F. Southern, M. E. Brezinski, and J. G. Fujimoto, ''*In vivo* cellular optical coherence tomography imaging,'' *Nat. Med.* **4**(7), 861–865 (1998).
75. G. J. Tearney, M. E. Brezinski, B. E. Bouma, S. A. Boppart, C. Pitris, and J. G. Fujimoto, ''*In vivo* endoscopic optical biopsy with optical coherence tomography,'' *Science* **276**(5321), 2037–2039 (1997).
76. J. G. Fujimoto, C. Pitris, S. A. Boppart, and M. E. Brezinski, ''Optical coherence tomography: an emerging technology for biomedical imaging and optical biopsy,'' *Neoplasia* **2**(1–2), 9–25 (2000).
77. B. E. Bouma, G. J. Tearney, C. C. Compton, and N. S. Nishioka, ''High-resolution imaging of the human esophagus and stomach *in vivo* using optical coherence tomography,'' *Gastrointest Endosc* **51**, 467–474 (2000).
78. M. V. Sivak, Jr., K. Kobayashi, J. A. Izatt, A. M. Rollins, R. Ung-Runyawee, A. Chak, R. C. Wong, G. A. Isenberg, and J. Willis, ''High-resolution endoscopic imaging of the GI tract using optical coherence tomography,'' *Gastrointest Endosc* **51**, 474–479 (2000).
79. X. Li, S. A. Boppart, J. Van Dam, H. Mashimo, M. Mutinga, W. Drexler, M. Klein, C. Pitris, M. L. Krinsky, M. E. Brezinski, and J. G. Fujimoto, ''Optical coherence tomography: advanced technology for the endoscopic imaging of Barrett's esophagus,'' *Endoscopy* **32**(12), 921–930 (2000).
80. B. E. Bouma, G. J. Tearney, H. Yabushita, M. Shishkov, C. R. Kauffman, D. DeJoseph Gauthier, B. D. MacNeill, S. L. Houser, H. T. Aretz, E. F. Halpern, and I. K. Jang, ''Evaluation of intracoronary stenting by intravascular optical coherence tomography,'' *Heart* **89**(3), 317–320 (2003).
81. S. A. Boppart, J. M. Herrmann, C. Pitris, D. L. Stamper, M. E. Brezinski, and J. G. Fujimoto, ''Real-time optical coherence tomography for minimally invasive imaging of prostate ablation,'' *Comput. Aided Surg.* **6**(2), 94–103 (2001).
82. Z. Chen, T. E. Milner, S. Srinivas, X. Wang, A. Malekafzali, M. J. C. van Gemert, and J. S. Nelson, ''Noninvasive imaging of *in vivo* blood flow velocity using optical Doppler tomography,'' *Opt. Lett.* **22**(14), 1119–1121 (1997).
83. J. A. Izatt, M. D. Kulkarni, S. Yazdanfar, J. K. Barton, and A. J.

Welch, ''*In vivo* bidirectional color Doppler flow imaging of picoliter blood volumes using optical coherence tomography,'' *Opt. Lett.* **22**(18), 1439–1441 (1997).
84. S. Yazdanfar, A. M. Rollins, and J. A. Izatt, ''Imaging and velocimetry of the human retinal circulation using color Doppler OCT,'' *Opt. Lett.* **25**(19), 1448–1450 (2000).
85. Y. Zhao, Z. Chen, C. Saxer, S. Xiang, J. F. De Boer, and J. S. Nelson, ''Phase-resolved optical coherence tomography and optical Doppler tomography for imaging blood flow in human skin with fast scanning speed and high velocity sensitivity,'' *Opt. Lett.* **25**(2), 114–116 (2000).
86. M. R. Hee, D. Huang, E. A. Swanson, and J. G. Fujimoto, ''Polarization-sensitive low-coherence reflectometer for birefringence characterization and ranging,'' *J. Opt. Soc. Am. A* **9**, 903–908 (1992).
87. J. F. De Boer, T. E. Milner, M. J. C. van Gemert, and J. S. Nelson, ''Two-dimensional birefringence imaging in biological tissue by polarization-sensitive optical coherence tomography,'' *Opt. Lett.* **22**, 934–936 (1997).
88. J. F. De Boer, T. E. Milner, and J. S. Nelson, ''Optical determination of the depth-resolved Stokes parameters of light backscattered from turbid media by use of polarization-sensitive optical coherence tomography,'' *Opt. Lett.* **24**, 300–302 (1999).
89. J. M. Schmitt, ''Optical coherence tomography (OCT): a review,'' *IEEE J. Sel. Top. Quantum Electron.* **5**(4), 1205–1215 (1999).
90. B. R. Masters, ''Selected papers on optical low-coherence reflectometry and tomography,'' *SPIE Press Milestone Series*, Bellingham, WA (2001).
91. B. E. Bouma and G. J. Tearney, *Handbook of Optical Coherence Tomography*, Marcel Dekker, New York (2002).
92. A. F. Fercher and C. K. Hitzenberger, ''Optical coherence tomography,'' *Prog. Opt.* **44**, 215–302 (2002).
93. A. F. Fercher, W. Drexler, C. K. Hitzenberger, and T. Lasser, ''Optical coherence tomography,'' *Rep. Prog. Phys.* **66**, 239–303 (2003).
94. J. G. Fujimoto, W. Drexler, U. Morgner, F. X. Kärtner, and E. P. Ippen, ''Optical coherence tomography: high resolution imaging using echoes of light,'' *Opt. Photonics News* **11**(1), 24–31 (2000).
95. M. D. Sherar, M. B. Noss, and F. S. Foster, ''Ultrasound backscatter microscopy images the internal structure of living tumour spheroids,'' *Nature (London)* **330**(6147), 493–495 (1987).
96. Z. Ding, H. Ren, Y. Zhao, J. S. Nelson, and Z. Chen, ''High resolution coherence tomography over a large depth range with an axicon lens,'' *Opt. Lett.* **27**(4), 234–245 (2002).
97. J. M. Schmitt, S. L. Lee, and K. M. Yung, ''An optical coherence microscope with enhanced resolving power in thick tissue,'' *Opt. Commun.* **142**, 203–207 (1997).
98. F. Lexer, C. K. Hitzenberger, W. Drexler, S. Molebny, H. Sattmann, M. Sticker, and A. F. Fercher, ''Dynamic coherent focus OCT with depth-independent transversal resolution,'' *J. Mod. Opt.* **46**(3), 541–553 (1999).
99. H. C. Howland and B. Howland, ''A subjective method for the measurement of monochromatic aberrations of the eye,'' *J. Opt. Soc. Am.* **67**, 1508–1518 (1977).
100. P. Artal and R. Navrro, ''High-resolution imaging of the living human fovea: measurement of the intercenter cone distance by speckle interferometry,'' *Opt. Lett.* **14**, 1098–1100 (1989).
101. E. J. Fernandez, I. Iglesias, and P. Artal, ''Closed-loop adaptive optics in the human eye,'' *Opt. Lett.* **26**(10), 746–748 (2001).
102. A. Roorda and D. R. Williams, ''The arrangement of the three cone classes in the living human eye,'' *Nature (London)* **397**, 520–522 (1999).
103. B. E. Bouma and G. J. Tearney, ''Power-efficient nonreciprocal interferometer and linear-scanning fiber-optic catheter for optical coherence tomography,'' *Opt. Lett.* **24**(8), 531–533 (1999).
104. A. M. Rollins and J. A. Izatt, ''Optimal interferometer designs for optical coherence tomography,'' *Opt. Lett.* **24**(21), 1484–1486 (2001).
105. G. L. Abbas, V. M. S. Chan, and T. K. Yee, ''Local-oscillator excess-noise suppression for homodyne and heterodyne detection,'' *Opt. Lett.* **8**(8), 419–421 (1983).
106. G. J. Tearney, B. E. Bouma, and J. G. Fujimoto, ''High-speed phase- and group-delay scanning with a grating-based phase control delay line,'' *Opt. Lett.* **22**, 1811–1813 (1997).
107. A. M. Rollins, M. D. Kulkarni, S. Yazdanfar, R. Ung-arunyawee, and J. A. Izatt, ''*In vivo* video rate optical coherence tomography,'' *Opt. Express* **3**(6), 219–229 (1998).
108. A. G. Podoleanu, J. A. Pogers, D. A. Jackson, and S. Dunne, ''Three dimensional OCT images from retina and skin,'' *Opt. Express* **23**7(9), 292–298 (2000).
109. S. Bourquin, P. Seitz, and R. P. Salathe, ''Optical coherence tomography based on a two-dimensional smart detector array,'' *Opt. Lett.* **26**(8), 512–514 (2001).
110. A. F. Fercher, C. K. Hitzenberger, G. Kamp, and S. Y. El-Zaiat, ''Measurement of intraocular distances by backscattering spectral interferometry,'' *Opt. Commun.* **117**(1–2), 43–48 (1995).
111. M. Wojtkowski, A. Kowalczyk, R. Leitgeb, and A. F. Fercher, ''Full range complex spectral optical coherence tomography technique in eye imaging,'' *Opt. Lett.* **27**(16), 1415–1417 (2002).
112. C. K. Hitzenberger and A. F. Fercher, ''Differential phase contrast in optical coherence tomography,'' *Opt. Lett.* **24**(9), 622–624 (1999).
113. M. Sticker, M. Pricher, E. Götzinger, H. Sattmann, A. F. Fercher, and C. K. Hitzenberger, ''En face imaging of single cell layers by differential phase-contrast optical coherence tomography,'' *Opt. Lett.* **27**(13), 1126–1128 (2002).
114. J. M. Schmitt, M. Yadlowsky, and R. F. Bonner, ''Subsurface imaging of living skin with optical coherence tomography,'' *Dermatology* **191**, 93–98 (1995).
115. J. M. Schmitt and A. Knuttel, ''Model of optical coherence tomography of heterogeneous tissue,'' *J. Opt. Soc. Am. A* **14**(6), 1231–1242 (1997).
116. A. M. Weiner, S. Oudin, D. E. Leaird, and D. H. Reitze, ''Shaping of femtosecond pulses using phase-only filters designed by simulated annealing,'' *J. Opt. Soc. Am. A* **10**(5), 1112–1120 (1993).
117. A. Apolonski, B. Považay, W. J. Wadsworth, J. C. Knight, P. St. J. Russel, and W. Drexler, ''Spectral shaping of supersontinuum in a cobweb photonic crystal fiber with sub-20 fs pulses,'' *J. Opt. Soc. Am. B* **19**, 2165 (2002).
118. A. F. Fercher, C. K. Hitzenberger, M. Sticker, E. Moreno-Barriuso, R. Leitgeb, W. Drexler, and H. Sattmann, ''A thermal light source technique for optical coherence tomography,'' *Opt. Commun.* **185**, 57–64 (2000).
119. L. Vabre, A. Dubois, and A. C. Boccata, ''Thermal full-field optical coherence tomography,'' *Opt. Lett.* **27**(7), 530–532 (2002).
120. H. H. Liu, P. H. Cheng, and J. Wang, ''Spatially coherent white light interferometer based on a point fluorescent source,'' *Opt. Lett.* **18**, 678–680 (1993).
121. X. Clivaz, F. Marquis-Weible, and R. P. Salathe, ''Optical low coherence reflectometry with 1.9 μm spatial resolution,'' *Electron. Lett.* **28**(16), 1553–1554 (1992).
122. A. M. Kowalevicz, T. Ko, I. Hartl, J. G. Fujimoto, M. Pollnau, and R. P. Salathe, ''Ultrahigh resolution optical coherence tomography using a superluminescent light source,'' *Opt. Express* **10**(7), 678–680 (2002).
123. http://www.superlumdiodes.com
124. Y. J. Rao, Y. N. Ning, and D. A. Jackson, ''Synthesized source for white-light sensing systems,'' *Opt. Lett.* **18**, 462–464 (1993).
125. D. N. Wang, Y. N. Ning, K. T. V. Grattan, A. W. Palmer, and K. Weir, ''Optimized multi wavelength combination sources for interferometric use,'' *Appl. Opt.* **33**, 7326–7333 (1994).
126. W. Drexler, C. K. Hitzenberger, A. Baumgartner, O. Findl, H. Sattmann, and A. F. Fercher, ''Multiple wavelength partial coherence interferometry,'' *Proc. SPIE* **2930**, 194–201 (1996).
127. A. Baumgartner, C. K. Hitzenberger, H. Sattmann, W. Drexler, and A. F. Fercher, ''Signal and resolution enhancements in dual-beam optical coherence tomography of the human eye,'' *J. Biomed. Opt.* **3**, 45–54 (1998).
128. A. M. Kowalevicz, T. R. Schibli, F. X. Kärtner, and J. G. Fujimoto, ''Ultralow-threshold Ker-lens mode-locked Ti:Al_2O_3 laser,'' *Opt. Lett.* **27**(2), 2037–2039 (2002).
129. S. Uemura and K. Torizuka, ''Generation of 10 fs pulses from a diode-pumped Kerr-lens mode-locked Cr:LiSAF laser,'' *Jpn. J. Appl. Phys.* **39**, 3472 (2000).
130. I. Sorokina, E. Sorokin, E. Wintner, A. Cassanho, H. P. Jensen, and R. Szipöcz, ''14-fs pulse generation in Kerr-lens mode-locked prismless Cr:LiSGaF and Cr:LiSAF lasers: observation of pulse self-frequency shift,'' *Opt. Lett.* **22**, 1716–1718 (1997).
131. P. C. Wagenblast, U. Morgner, F. Grawert, T. R. Schibli, F. X. Kärtner, V. Scheuer, G. Angelow, and M. J. Lederer, ''Generation of sub-10-fs pulses from a Kerr-lens mode-locked Cr 3+:LiCAF laser oscillator by use of third-order dispersion-compensating double-chirped mirrors,'' *Opt. Lett.* **27**, 1726–1728 (2002).
132. B. E. Bouma, G. J. Tearney, S. A. Boppart, M. R. Hee, M. E. Brez-

inski, and J. G. Fujimoto, ''High-resolution optical coherence tomographic imaging using a mode-locked Ti-Al_2O_3 laser source,'' *Opt. Lett.* **20**(13), 1486–1488 (1995).
133. W. Drexler, U. Morgner, F. X. Kärtner, C. Pitris, S. A. Boppart, X. D. Li, E. P. Ippen, and J. G. Fujimoto, ''*In vivo* ultrahigh resolution optical coherence tomography,'' *Opt. Lett.* **24**(17), 1221–1223 (1999).
134. U. Morgner, F. X. Kärtner, S. H. Cho, Y. Chen, H. A. Haus, J. G. Fujimoto, E. P. Ippen, V. Scheuer, G. Angelow, and T. Tschudi, ''Sub-two-cycle pulses from a Kerr-lens mode-locked Ti:sapphire laser,'' *Opt. Lett.* **24**(6), 411–413 (1999).
135. W. Drexler, U. Morgner, R. K. Ghanta, J. S. Schuman, F. X. Kärtner, M. R. Hee, E. P. Ippen, and J. G. Fujimoto, ''New technology for ultrahigh resolution optical coherence tomography of the retina,'' in *The Shape of Glaucoma, Quantitative Neural Imaging Techniques*, H. Lemij and J. S. Schuman, Eds., pp. 75–104, Kugler Publications, The Hauge, The Netherlands (2000).
136. W. Drexler, U. Morgner, R. K. Ghanta, J. S. Schuman, F. X. Kärtner, and J. G. Fujimoto, ''Ultrahigh resolution ophthalmologic optical coherence tomography,'' *Nat. Med.* **7**(4), 502–507 (2001).
137. M. Glosmann, B. Hermann, C. Schubert, H. Sattmann, P. K. Ahnelt, and W. Drexler, ''Histological correlation of pig retina radial stratification with ultrahigh resolution optical coherence tomography,'' *Invest. Ophthalmol. Visual Sci.* **44**(4), 1696–1703 (2003).
138. W. Drexler, H. Sattman, B. Hermann, T. H. Ko, M. Stur, A. Unterhuber, C. Scholda, O. Findl, M. Wirtitsch, J. G. Fujimoto, and A. F. Fercher, ''Enhanced visualization of macular pathology using ultrahigh resolution optical coherence tomography,'' *Arch. Ophthalmol. (Chicago)* **121**, 695–706 (2003).
139. A. Unterhuber, B. Hermann, H. Sattmann, B. Povazay, W. Drexler, G. Tempea, V. Yakovlev, C. Schubert, E. M. Anger, P. K. Ahnelt, M. Stur, J. E. Morgan, T. Le, and A. Stingl, ''Compact, low cost Ti:Al_2O_3 laser for *in vivo* ultrahigh resolution optical coherence tomography,'' *Opt. Lett.* **28**(11), 905–907 (2003).
140. J. M. Schmitt, A. Knuttel, M. Yadlowsky, and M. A. Eckhaus, ''Optical-coherence tomography of a dense tissue: statistics of attenuation and backscattering,'' *Phys. Med. Biol.* **39**, 1705–1720 (1994).
141. B. E. Bouma, G. J. Tearney, I. P. Bilinsky, B. Golubovic, and J. G. Fujimoto, ''Self phase modulated Kerr-lens mode locked Cr:forsterite laser source for optical coherent tomography,'' *Opt. Lett.* **21**, 1839–1841 (1996).
142. C. Chudoba, J. G. Fujimoto, E. P. Ippen, H. A. Haus, U. Morgner, F. X. Kärtner, V. Scheuer, G. Angelow, and T. Tschudi, ''All-solid-state Cr:forsterite laser generating 14-fs pulses at 1.3 μm,'' *Opt. Lett.* **26**(5), 292–294 (2001).
143. J. K. Ranka, R. S. Windeler, and A. J. Stentz, ''Visible continuum generation in air-silica microstructure optical fibers with anomalous dispersion at 800 nm,'' *Opt. Lett.* **25**(1), 25–27 (2000).
144. T. A. Birks, W. J. Wadsworth, and P. St. J. Russel, ''Generation of an ultra-broad supercontimuum in tapered fibers,'' *Opt. Lett.* **25**(19), 1415–1417 (2000).
145. I. Hartl, X. D. Li, C. Chudoba, R. K. Ghanta, T. K. Ko, J. G. Fujimoto, J. K. Ranka, and P. S. Windeler, ''Ultrahigh resolution optical coherence tomography using continuum generation in an air-silica microstructure optical fiber,'' *Opt. Lett.* **26**, 608–610 (2001).
146. K. Bizheva, B. Povazay, B. Hermann, H. Sattmann, W. Drexler, M. Mei, R. Holzwarth, T. Hoelzenbein, V. Wacheck, and H. Pehamberger, ''A compact, broad bandwidth fiber laser for sub-2 μm axial resolution optical coherence tomography in the 1300 nm wavelength region,'' *Opt. Lett.* **28**, 707–709 (2003).
147. B. E. Bouma, L. E. Nelson, G. J. Tearney, D. J. Jones, M. E. Brezinski, and J. G. Fujimoto, ''Optical coherence tomography imaging of human tissue at 1.55 μm and 1.81 μm using Er- and Tm-doped fiber sources,'' *J. Biomed. Opt.* **3**(1), 76–79 (1998).
148. D. J. Ripin, C. Chudoba, J. T. Gopinath, J. G. Fujimoto, E. P. Ippen, U. Morgner, F. X. Kärtner, V. Scheuer, G. Angelow, and T. Tschudi, ''Generation of 20-fs pulses by prismless Cr^{4+}:YAG laser,'' *Opt. Lett.* **27**(1), 61–63 (2002).
149. M. Seefeldt, A. Heuer, and R. Menzl, ''Compact white-light source with an average output power of 2.4 W and 900 nm spectral bandwidth,'' *Opt. Commun.* **216**, 199–202 (2003).
150. B. Povazay, K. Bizheva, B. Hermann, A. Unterhuber, H. Sattmann, A. F. Fercher, W. Drexler, C. Schubert, P. K. Ahnelt, M. Mei, R. Holzwarth, W. Wadsworth, J. Knight, and P. Russell, ''Ultrahigh resolution ophthalmic optical coherence tomography with enhanced penetration,'' *Opt. Express.* **11**(17), 1980–1986 (2003).
151. Y. Wang, Y. Zhao, J. S. Nelson, and Z. Chen, ''Ultrahigh-resolution optical coherence tomography by broadband continuum generation from a photonic crystal fiber,'' *Opt. Lett.* **28**(3), 182–184 (2003).
152. B. Povazay, K. Bizheva, A. Unterhuber, B. Hermann, H. Sattmann, A. F. Fercher, W. Drexler, A. Apolonski, W. Wadsworth, J. Knight, P. Russell, M. Vetterlein, and E. Scherzer, ''Submicrometer axial resolution optical coherence tomography,'' *Opt. Lett.* **27**, 1800 (2002).
153. M. D. Kulkarni and J. A. Izatt, ''Spectroscopic optical coherence tomography,'' CLEO '96. Summaries of papers presented at the Conference on Lasers and Electro Optics 9 (96CH35899), pp. 59–60, Optical Society of America (1996).
154. J. M. Schmitt, S. H. Xiang, and K. M. Yung, ''Differential absorption imaging with optical coherence tomography,'' *J. Opt. Soc. Am. A* **15**(9), 2288–2296 (1998).
155. U. S. Sathyam, B. W. Colston, B. M. DaSilva, and M. J. Everett, ''Evaluation of optical coherence quantitation of analytes in turbid media by use of two wavelengths,'' *Appl. Opt.* **38**, 2097–2104 (1999).
156. J. L. Boulnois and A. Morfino, ''Photo-bimolecular effects of laser radiation,'' *Minerva Med.* **74**(27), 1669–1673 (1983).
157. U. Morgner, W. Drexler, F. X. Kärtner, X. D. Li, C. Pitris, E. P. Ippen, and J. G. Fujimoto, ''Spectroscopic optical coherence tomography,'' *Opt. Lett.* **25**(2), 111–113 (2000).